

2019

Color-Ratio Based Strawberry Plant Localization and Nutrition Deficiency Detection

Xiangling Kong
University of Central Florida

 Part of the [Mechanical Engineering Commons](#)

Find similar works at: <https://stars.library.ucf.edu/etd>

University of Central Florida Libraries <http://library.ucf.edu>

This Doctoral Dissertation (Open Access) is brought to you for free and open access by STARS. It has been accepted for inclusion in Electronic Theses and Dissertations by an authorized administrator of STARS. For more information, please contact STARS@ucf.edu.

STARS Citation

Kong, Xiangling, "Color-Ratio Based Strawberry Plant Localization and Nutrition Deficiency Detection" (2019). *Electronic Theses and Dissertations*. 6518.

<https://stars.library.ucf.edu/etd/6518>

COLOR-RATIO BASED STRAWBERRY PLANT LOCALIZATION AND NUTRITION
DEFICIENCY DETECTION

by

XIANGLING KONG

M.S. Beijing Union University, China, 2014

B.S. Beijing Union University, China, 2007

A dissertation submitted in partial fulfilment of the requirements
for the degree of Doctor of Philosophy
in the Department of Mechanical and Aerospace Engineering
in the College of Engineering and Computer Science
at the University of Central Florida
Orlando, Florida

Summer Term
2019

Major Professor: Yunjun Xu

© 2019 Xiangling Kong

ABSTRACT

In recent years, precision agriculture has become popular anticipating to partially meet the needs of an ever-growing population with limited resources. Plant localization and nutrient deficiency detection are two important tasks in precision agriculture. In this dissertation, these two tasks are studied by using a new color-ratio (C-R) index technique. Firstly, a low cost and light scene invariant approach is proposed to detect green and yellow leaves based on the color-ratio (C-R) indices. A plant localization approach is then developed using the relative pixel relationships of adjacent plants. Secondly, the Sobel operator and morphology techniques are applied to segment the target strawberry leaf from a field image. The characterized color for a specific nutrient deficiency is detected by the C-R indices. The pattern of the detected color on the leaf is then examined to determine the specific nutrient deficiency. The proposed approaches are validated in a commercial strawberry farm.

Dedicated to my family and friends.

ACKNOWLEDGMENTS

I would like to express my deepest and sincerely appreciation to my supervisor, Dr. Yunjun Xu, for his dedication and inspiration. It is his guidance, timely advice, and meticulous scrutiny helped me to accomplish dissertation.

I would also like to thank my current and former committee members, Dr. Tarek Elgohary, Dr. Qiushi Fu, Dr. Dazhong Wu, Dr. Liqiang Wang, and Dr. Adan Vela.

I am deeply grateful to my former and current lab mates in Autonomous Robotics and Control Laboratory (ArcLab), Dr. Douglas Freese, Dr. Sinem Defterli, Dr. Ni Li, Dr. He Shen, Andong Dai, Qiang Li, August Mark, and Jonah Mapes, for their team work and support throughout my study.

Special thanks are given to my families for their immense love and support in my entire life. I also would like to give my special appreciation to my husband, Wei Lv, for his love and encouragement.

TABLE OF CONTENTS

LIST OF FIGURES	x
LIST OF TABLES	xiii
CHAPTER 1: INTRODUCTION	1
Motivation and Literature Review	1
Strawberry Plant Localization	1
Plant Alive Status Detection	2
Plant Nutrient Deficiency Detection	3
Contributions	4
Dissertation Outline	4
CHAPTER 2: COLOR-RATIO INDICES	6
Definitions of Color-Ratio Indices	6
Simulation Validation of C-R Indices	15
CHAPTER 3: STRAWBERRY PLANT ALIVE STATUS DETECTION	18
Problem Definition	18

Plant Alive Status Detection	18
Leaf Detection	18
Plant Alive Status Detection	19
Experimental Validation	19
Strawberry Leaf Detection via C-R Indices	19
Plant Alive Status Detection	20
CHAPTER 4: STRAWBERRY PLANT LOCALIZATION VIA RELATIVE PIXEL	24
Problem Definition	24
Plant Localization via Relative Pixel Position	25
Process Model	25
Measurement Model	26
Experiment Validation and Discussions	33
Experiment Settings	33
Plant Localization Validation	34
CHAPTER 5: Strawberry Plant Nutrient Deficiency Detection	38
Problem Definition	39
Nutrient Deficiency Detection	40

Leaf Segmentation with Sobel Operator	40
Nutrient Deficiency Symptom Pattern Recognition	42
Nutrient Deficiency Color Feature Recognition	42
Color Distribution Pattern Recognition	45
Nutrient Deficiency Detection via Leaf Feature Extraction	46
Experimental Validation	50
Experiment Setting	50
Nutrient Deficiency Symptom Pattern Recognition	50
Nutrient Deficiency Detection via Leaf Feature Extraction	50
CHAPTER 6: IMPROVED CONTROL AFFINE, APPROXIMATED WHEEL TERRAIN	
INTERACTION MODEL FOR A GROUND SCOUTING ROBOT	52
Terramechanics WTIM Simulation	52
Approximated Wheel Terrain Interaction Model	54
Approximated Control Affine Model	56
States and Unknown Parameters Estimation	57
Experiment Validation	59
Experiment Validation	60

CHAPTER 7: CONCLUSION AND FUTURE WORK	69
Conclusions	69
Future Work	70
APPENDIX A: PARTIAL DERIVATIVE MATRICES OF RELATIVE PIXEL POSITION IN THE EKF	71
LIST OF REFERENCES	82

LIST OF FIGURES

Figure 3.1: Leaf detection using the C-R indices in different times of a day (The pictures are captured from the Pappy's Patch, Orlando, FL, on Nov. 3 rd , 2018)	21
Figure 3.2: Leaf detection using the C-R indices in different weather conditions (The images are captured from the Pappy's Patch, Orlando, FL, on Oct. 30 th , 2018, Oct. 23 th , 2018, and Oct. 26 th , 2018, respectively)	22
Figure 3.3: Leaf detection using the C-R indices in different growing stages (The images are captured from the Pappy's Patch, Orlando, FL, on Nov. 3 rd , 2018, Dec. 1 st , 2017, and Mar. 12 th , 2018, respectively)	23
Figure 4.1: The procedure of plant alive status detection and localization	24
Figure 4.2: The coordinates of the field robot	26
Figure 4.3: The ground robot in a strawberry farm	34
Figure 4.4: The measured and estimated relative positions of adjacent plants. (a) Relative positions in the x direction, and (b) relative position in the y direction. The squared line and the stared line represent the measurements and the estimates, respectively	35
Figure 4.5: The errors between the measured and estimated relative positions. (a) The error in the x direction, and (b) the error in the y direction	36

Figure 4.6: The measured and estimated absolute positions of the strawberry plants in the field. The squared line and the stared line represent the measurements and the estimates, respectively	36
Figure 4.7: The errors of the measured and estimated absolute positions. (a) The error in the x direction, and (b) the error in the y direction	37
Figure 5.1: Deficiencies on strawberry leaf. (a)-(c) are provided by Dr. Shinsuke Agehara from the University of Florida, and (d)-(f) are captured from the Pappy's Patch in Orlando, FL and labeled by Dr. Shinsuke Agehara from the University of Florida	39
Figure 5.2: The procedure of the proposed nutrient deficiency detection method	40
Figure 5.3: The 3x3 kernels of Sobel operator. The images are cited from [11,53]	41
Figure 5.4: The C-R indices of the scorch and purple pixels of strawberry deficiency: (a) the M index, (b) the N index, and (c) the K index.	43
Figure 5.5: The R , G , and B values of the scorch and purple pixels of strawberry deficiency: (a) the R value, (b) the G value, and (c) the B value.	44
Figure 5.6: The C-R indices of the healthy green and yellow-green pixels of strawberry leaves: (a) the M index, (b) the N index, and (c) the K index.	45
Figure 5.7: The definition of the distribution area of nutrient deficiency	46

Figure 5.8: Strawberry plant nutrient deficiency detection using the proposed approach. (a) A leaflet in the field, (b) the segmented leaf using the Sobel operator, and (c) the characterized colors and their locations. The image is captured from Pappy's Patch on Feb. 23, 2019.	49
Figure 6.1: Longitudinal reaction force simulated using the full WTIM with a torus shape.	53
Figure 6.2: Lateral reaction force simulated using the full WTIM with a torus shape. . . .	53
Figure 6.3: DDAGR In Field	60
Figure 6.4: A scouting path covering three rows in a commercial strawberry farm. . . .	61
Figure 6.5: Measured and estimated wheel velocities of DDAGR in the scouting motion: (a) left wheel angular velocity and (b) right wheel angular velocity. The dotted and solid lines represent the measurement and estimation, respectively.	65
Figure 6.6: Measured and estimated velocities of DDAGR in the scouting motion: (a) longitudinal velocity, (b) lateral velocity, and (c) yaw rate, where the dotted and solid lines represent the measurement and estimation, respectively. . . .	66
Figure 6.7: Turn Wheel Bank Velocities	67
Figure 6.8: Turn Wheel Bank Velocities	67
Figure 6.9: Parameter estimation of DDAGR approximated WTIM in the scouting mo- tion: \hat{c}_0 , \hat{c}_1 , \hat{c}_2 , \hat{c}_3 , and \hat{c}_4 are the parameters in the longitudinal force model; while \hat{d}_1 , \hat{d}_2 , and \hat{d}_3 are the parameters in the lateral force model.	68

LIST OF TABLES

Table 1.1: Leaflet symptoms when the strawberry experiencing N, P, and K deficiencies .	5
Table 2.1: Sensitivity and specificity analyses on the greenness detection	17
Table 2.2: Sensitivity and specificity analyses on the yellowness detection	17
Table 2.3: Sensitivity and specificity analyses on the reddish detection	17
Table 5.1: Nutrient deficiency color and color distribution pattern inspection by using the C-R indices	48
Table 5.2: Performance of the nutrition deficiency detection approach in strawberry leaflets	51
Table 6.1: Goodness of fit for the longitudinal force in the approximated WTIM	55
Table 6.2: Goodness of fit for the lateral force in the approximated WTIM	56
Table 6.3: Wheel bank velocities used in the scouting motion experiment	63

CHAPTER 1: INTRODUCTION

Motivation and Literature Review

Higher efficiency in agricultural productions can partially meet the needs of world growing population and the demands of a better life quality. With a limited amount of land available for cultivation, precision agriculture has become increasingly important and its economic impact is expected to reach \$43.4 billion by 2025 [1]. In precision agriculture, regularly monitoring fields provides growers opportunities to track plant growth, assess plant health, and predict crop yields. However, for large size agricultural fields, it is labor intensive for human inspectors to conduct regular monitoring. Autonomous robots equipped with a suite of sensors can collect more data per unit time compared with human inspectors. In addition to the benefit of being less labor dependent, routine robotic scouting throughout agricultural fields will lead to higher result repeatability [2].

Strawberry Plant Localization

One important task in precision agriculture is plant localization. The methods used in plant localization can be categorized into local and global techniques [3, 4], based on whether or not prior knowledge of target initial positions is available [5–7]. As a local method, geo-referencing relates the pixel positions of plants in images to their geographic coordinates. The challenges associated with the geo-referencing methods derive from inaccurate plant identification and position uncertainties. Sometimes in the planting stage, Real Time Kinematic Global Positioning System (RTK-GPS) and absolute shaft encoders are used to record the plant positions, and the position error is at the centimeter level [8]. However, the performance degrades if the surrounding environment is disturbed by plants and varying terrain. Additionally, the use of GPS to locate each plant can be

labor intensive, especially for routine operations. LiDAR is used to detect and locate trees with a 95.7% accuracy [9]. The LiDAR approach is, however, expensive, bulky, and difficult to maintain.

Plant Alive Status Detection

A plant is alive or not can be easily done by human inspectors via its color. For example, in strawberry fields, alive leaves are green, while others will turn yellow. This relatively simple task for humans can be quite challenging for robots due to varying light scenes. To date, autonomous color detection is mainly accomplished using wave length-based or pixel-based algorithms. The green color reflects the light with a wavelength between 500 nm and 570 nm, whereas the wavelength of yellow color is between 570 nm and 590 nm [10, 11]. However, wave length-based spectrometers are expensive and have many stringent requirements (e.g., distance, orientation, field of view, and light intensity), making them non-ideal and sometimes impossible for use in autonomous field robots [12, 13]. Pixel-based algorithms do not have those stringent requirements as wavelength-based approaches. The RGB (red, green, and blue) or HSV (hue, saturation, and value) color models [11] are two mainstream models used in detecting colors with proper threshold values [14–16]. For example, multilevel thresholds are used in the R, G, and B color channels for segmenting target objects from their background [17]. The HSV color model can properly decouple color and gray-scale information. For example, in [18], the hue values are used to separate the background from green plants. The disadvantages of these pixel-based methods are as follows. (1) The HSV color model has singularities in its nonlinear transformation. (2) Threshold values for both methods are sensitive to varying light scenes. Sometimes neural network [19] or fuzzy logic [20, 21] methods are applied to enhance the robustness of color detection under different light scenes. Although they have shown promising results in some applications, their inherent issues cannot be avoided. For example, they need a large amount of training data and it is practically impossible to cover all light scenes. Additionally, no theoretical proof in general is available for those methods.

Plant Nutrient Deficiency Detection

A balanced nutrient is crucial for crops to grow. Short or excessive nutrient supply will lead to significant premature crop death and yield loss [22]. Routine nutrient deficiency inspection can help farmers and growers assess the nutrient status in crops and apply rescue treatments timely. Usually visual inspection of growing crops is the first indicator when the crops experience any nutrient deficiency [23]. Crops with nutrient deficiency may show different symptoms. For example corns with the potassium deficiency often have yellow and scorch leaf edges in their lower parts [24,25]. Purple leaves may indicate a phosphorus deficiency in tomatoes [26,27]. Uniform pale green on strawberry leaves means a nitrogen deficiency [28,29]. However, conducting nutrient inspection requires expertise, is time consuming and labor intensive [23], especially in large farms. Visual inspection with autonomous scouting robots not only can speed up the inspection process, reduce labor cost, but also provide farmers and growers with potential fertility issue information throughout their farms.

The fact that different symptoms may appear on different parts of crops can be used to identify certain nutrient deficiencies, especially for those symptoms shown on leaflets. For strawberry crops, nitrogen (N), phosphorus (P), and potassium (K) are the key chemical elements [30]. As shown in Table 1.1, nitrogen deficiency turns strawberry leaves from green to light green then to yellow. Purpling is often the indicator of phosphorus deficiency. The potassium deficiency frequently leads to scorch leaf margins on mature leaflets.

There is an extensive amount of research has been conducted on crop deficiency detection using hyperspectral cameras [31]. For example, hyperspectral images are used to analyze the total nitrogen contents in pepper crops [32], and the reflectance spectra of the nitrogen concentration is studied in [33]. However, the high cost and the strict operation environment requirements make this application hard in practice by autonomous robots in fields.




Contributions

The contributions of the study have three folds. Firstly, the distinct C-R index ranges can be used to differentiate the green, yellow, and red colors, instead of using the values of hue, saturation, and value in the HSV color model. This method is shown to be robust under various light scenes. Furthermore, the leaf color detection method using the proposed C-R indices is conducted in the RGB color space, which avoids the transformation between different color models and leads to more efficient calculations. As compared with spectrometer approaches, the proposed color detection method via RGB cameras is low cost and has minimal requirements for routine operations. Secondly, a low cost and lightweight plant localization method is proposed to be used in field robots. Here, the relative pixel positions of plants are used to predict both the relative and absolute positions of plants. Such a differential style method can reach the same level of accuracy as a LiDAR, but with a much lower upfront and maintenance cost. Thirdly, a low-cost method is introduced to inspect strawberry crops' nutrient deficiencies. The C-R indices are applied to extract the deficiency color features from leaf images. Such low-cost and lightweight method can be easily applied by a ground robot and increase the efficiency in routine field operations.

Dissertation Outline

The dissertation is organized as follows. In Chapter 2, a color-ratio (C-R) index is introduced and proven to be robust with respect to various light scenes. In Chapter 3, the proposed C-R index is applied to detect the alive status of strawberry plants. In Chapter 4, a plant localization algorithm is developed. In Chapter 5, a nutrient deficiency detection algorithm is proposed. In Chapter 6, an improved control affine, approximated wheel terrain interaction model for a scouting robot is presented. The conclusions and future works are discussed in the end.

Table 1.1: Leaflet symptoms when the strawberry experiencing N, P, and K deficiencies

Deficiency	Leaflet Symptom [[34]]	Leaflet Image
Nitrogen N	<ul style="list-style-type: none"> • Young Leaflet: Starting from light green to yellowing; • Mature leaflet: uniform yellowing with reddish from the margins 	 <p>(The image is captured from Pappy's Patch, Orlando, FL)</p>
Phosphorus (P)	Purpling from the margin	 <p>(The image is provided by Dr. Shinsuke Agehara from University of Florida)</p>
Potassium (K)	Scorch on the margins	 <p>(The image is provided by Dr. Shinsuke Agehara from University of Florida)</p>

CHAPTER 2: COLOR-RATIO INDICES

This work appeared in [35], from Kong, X. and Xu, Y., Strawberry Plant Alive Status Detection and Relative Pixel Based Plant Localization, submitted to the ASME Journal of Dynamic System, Measurement, and Control in Jan, 2019.

Definitions of Color-Ratio Indices

Definition 1. *The varying light scenes in this study include but are not limited to light conditions in different time of a day (morning, noon, or afternoon), shadow, weather, and season, as well as different growing stages of plant .*

Assumption 1. *Based on [36, 37], all the light scenes mentioned in Definition 1 can be captured within the saturation $S \in [0, 1]$ and the value $V \in [0, 1]$ in the HSV color model.*

Definition 2. *(Green Pixel) The pixel is considered to be “green” if its hue value is within the range of $(60^\circ, 180^\circ]$ [38].*

Definition 3. *(Yellow Pixel) The pixel is considered to be “yellow” if its hue value is within the range of $(30^\circ, 60^\circ]$ [38].*

Definition 4. *(Red Pixel) The pixel is considered to be “red” if its hue value is within the range of $(0^\circ, 30^\circ]$ [38].*

Definition 5. *The color-ratio (C-R) indices are defined as*

$$M = R/G \tag{2.1}$$

$$N = B/G \quad (2.2)$$

and

$$K = B/R \quad (2.3)$$

, where $R \in [0, 255]$, $G \in [0, 255]$, and $B \in [0, 255]$ represent the values of red, green, and blue, respectively, in the RGB color model.

Lemma 1. *The color of pixel P is “green” if and only if the C-R index ranges of the pixel satisfy $M \in [0, 1]$, $N \in [0, 1]$, and $K \in [0, \infty)$.*

Proof. Sufficient condition. According to Definition 2, the hue value is within the range of $H \in (60^\circ, 180^\circ]$ [38]. As mentioned in Assumption 1, $S \in [0, 1]$ and $V \in [0, 1]$ cover all aforementioned light scenes.

Case 1: When $H \in (60^\circ, 120^\circ]$, the values of R , G , and B of pixel P in the RGB color model can be transformed from the HSV model using [36, 37]

$$R = X + V - C \quad (2.4)$$

$$G = V \quad (2.5)$$

and

$$B = V - C \quad (2.6)$$

, where

$$C \triangleq VS \quad (2.7)$$

and

$$X \triangleq C (1 - |H' \bmod 2 - 1|) \quad (2.8)$$

In Eq. (2.8), H' is the hue index and defined as $H' = H/60^\circ$. Since the hue of pixel P is in the range of $(60^\circ, 120^\circ]$. With Definition 5 and Eqs. (2.4-2.6), the C-R indices of pixel P can be derived as

$$\begin{aligned} M &= (X + V - C) / V \\ &= [VS (1 - |H' \bmod 2 - 1|) + V - VS] / V \\ &= S (1 - |H' \bmod 2 - 1|) + 1 - S \\ &= 1 - S |H' \bmod 2 - 1| \end{aligned} \quad (2.9)$$

$$N = (V - C) / V = (V - VS) / V = 1 - S \quad (2.10)$$

and

$$\begin{aligned} K &= (V - C) / (X + V - C) \\ &= (V - VS) / [VS (1 - |H' \bmod 2 - 1|) + V - VS] \\ &= (1 - S) / (1 - S |H' \bmod 2 - 1|) \end{aligned} \quad (2.11)$$

Since $H' \in (1, 2]$, $0 < |H' \bmod 2 - 1| \leq 1$. Additionally, because $S \in [0, 1]$, $0 \leq S |H' \bmod 2 - 1| \leq S \leq 1$ and $0 \leq 1 - S \leq 1 - S |H' \bmod 2 - 1| \leq 1$. Thus, $M \in [0, 1]$, $N \in [0, 1]$, and $K \in [0, 1]$.

Case 2: When $H \in (120^\circ, 180^\circ]$, the values of R , G , and B of pixel P in the RGB color model

can be transformed from the HSV model [36, 37] using

$$R = V - C \quad (2.12)$$

$$G = V \quad (2.13)$$

and

$$B = X + V - C \quad (2.14)$$

Since the hue of pixel P is in the range of $(120^\circ, 180^\circ]$, with Definition 5 and Eqs. (2.7-2.8, 2.12-2.14), the C-R indices of pixel P can be derived as

$$M = (V - C) / V = (V - VS) / V = 1 - S \quad (2.15)$$

$$\begin{aligned} N &= (X + V - C) / V \\ &= [VS(1 - |H' \bmod 2 - 1|) + V - VS] / V \\ &= S(1 - |H' \bmod 2 - 1|) + 1 - S \\ &= 1 - S |H' \bmod 2 - 1| \end{aligned} \quad (2.16)$$

and

$$\begin{aligned} K &= (X + V - C) / (V - C) \\ &= [VS(1 - |H' \bmod 2 - 1|) + V - VS] / (V - VS) \\ &= (1 - S |H' \bmod 2 - 1|) / (1 - S) \end{aligned} \quad (2.17)$$

Since $H' \in (2, 3]$, $0.5 \leq |H' \bmod 2 - 1| < 1$. Additionally, because $S \in [0, 1]$, $0 \leq S |H' \bmod 2 - 1| < 1$. Therefore, $M \in [0, 1]$, $N \in (0, 1]$, and $K \in [0, \infty)$. Combining Case 1 and Case 2, the C-R

indices are within the ranges of $M \in [0, 1]$, $N \in [0, 1]$, and $K \in [0, \infty)$ if the color of pixel P is “green”.

Necessary condition. Case 1: when the C-R index ranges of pixel P are $M \in [0, 1]$, $N \in [0, 1]$, and $K \in [0, 1]$. According to Definition 5, the values of R , G , and B satisfy the relationship of $0 \leq B \leq R \leq G$. The hue index H' can be calculated [39] as

$$H' = (B - R) / (C_{p,max} - C_{p,min}) + 2 \quad (2.18)$$

, where $C_{p,max}$ and $C_{p,min}$ are the maximum and minimum color components of pixel P in the RGB color model. In this case, $C_{p,max} = G$ and $C_{p,min} = B$. Thus, in Eq. (2.18),

$$-1 < (B - R) / (C_{p,max} - C_{p,min}) = (B - R) / (G - B) \leq 0 \quad (2.19)$$

and

$$1 < (B - R) / (G - B) + 2 \leq 2 \quad (2.20)$$

The hue index H' of pixel P is in the range of $H' \in (60^\circ, 120^\circ]$. According to [39], the saturation S and the value V can be calculated using

$$S = (C_{p,max} - C_{p,min}) / C_{p,max} = (G - B) / G \quad (2.21)$$

and

$$V = C_{p,max} / 255 = G / 255 \quad (2.22)$$

, where $G \in [0, 255]$ and $B \in [0, 255]$. Thus $S \in [0, 1]$ and $V \in [0, 1]$, respectively, can be derived, which imply that all the aforementioned light scenes in Definition 1 are covered.

Case 2: when the C-R index ranges of pixel P are $M \in [0, 1]$, $N \in [0, 1]$, and $K \in (1, \infty)$. According to Definition 5, the values of R , G , and B satisfy the relationship of $0 \leq R < B \leq G$. The hue index H' can be calculated [39], and the maximum and minimum color components of pixel P in the RGB color model are $C_{p,max} = G$ and $C_{p,min} = R$. Then

$$0 < (B - R) / (C_{p,max} - C_{p,min}) = (B - R) / (G - R) \leq 1 \quad (2.23)$$

and

$$2 < (B - R) / (G - B) + 2 \leq 3 \quad (2.24)$$

The hue index H' can be derived within the range of $H' \in (2, 3]$, and the hue of pixel P can be determined within the range of $(120^\circ, 180^\circ]$. According to [39], the saturation S and the value V can be calculated using

$$S = (C_{p,max} - C_{p,min}) / C_{p,max} = (G - R) / G \quad (2.25)$$

and

$$V = C_{p,max} / 255 = G / 255 \quad (2.26)$$

Thus, we can derive that $S \in [0, 1]$ and $V \in [0, 1]$, respectively, which imply that all the aforementioned light scenes in Definition 1 are covered. Combining Case 1 and Case 2, the hue value of pixel P is in the range of $(60^\circ, 180^\circ]$. According to Definition 2, the color of the pixel can be determined as ‘green’. \square

Lemma 2. *The color of pixel P is ‘yellow’ if and only if the C-R index ranges of the pixel satisfy $M \in [1, 2)$, $N \in [0, 1]$, and $K \in [0, 1]$.*

Proof. **Sufficient condition.** According to Definition 3, the hue value is within the range of $H \in$

$(30^\circ, 60^\circ]$. To cover all light scenes in Definition 1, $S \in [0, 1]$ and $V \in [0, 1]$. The R , G , and B values of pixel P in the RGB color model can be transformed from the HSV model using [36, 37]

$$R = V \quad (2.27)$$

$$G = X + V - C \quad (2.28)$$

$$B = V - C \quad (2.29)$$

Since the hue of pixel P is in the range $H \in (30^\circ, 60^\circ]$, $H' \in (0.5, 1]$. With Definition 5 and Eqs. (2.7, 2.8, 2.27-2.29), the color ratios M , N , and K of pixel P can be derived as

$$\begin{aligned} M &= V / (X + V - C) \\ &= V / [VS(1 - |H' \bmod 2 - 1|) + V - VS] \\ &= 1 / [S(1 - |H' \bmod 2 - 1|) + 1 - S] \\ &= 1 / (1 - S |H' \bmod 2 - 1|) \end{aligned} \quad (2.30)$$

$$\begin{aligned} N &= (V - C) / (X + V - C) \\ &= (V - VS) / [VS(1 - |H' \bmod 2 - 1|) + V - VS] \\ &= (1 - S) / [S(1 - |H' \bmod 2 - 1|) + 1 - S] \\ &= (1 - S) / (1 - S |H' \bmod 2 - 1|) \end{aligned} \quad (2.31)$$

and

$$K = (V - C) / V = (V - VS) / V = (1 - S) \quad (2.32)$$

Since $H' \in (0.5, 1]$, $0 \leq |H' \bmod 2 - 1| < 0.5$. Additionally, because $S \in [0, 1]$, $0 \leq |H' \bmod 2 - 1| < 0.5$. Thus, the C-R indice are within the ranges of $M \in [1, 2)$, $N \in [0, 1]$, and $K \in [0, 1]$.

Necessary condition. According to Definition 5, if the C-R index ranges of pixel P are $M \in [1, 2)$, $N \in [0, 1]$, and $K \in [0, 1]$, the R , G , and B values satisfy the relationships of $0 \leq B \leq G \leq R$ and $R < 2G$. The hue index H' can be calculated as [39]

$$H' = [(G - B) / (C_{p,max} - C_{p,min})] \bmod 6 \quad (2.33)$$

The maximum and minimum color components are $C_{p,max} = R$ and $C_{p,min} = B$, respectively. According to Eq. (2.33),

$$(G - B) / (C_{p,max} - C_{p,min}) = (G - B) / (R - B) \quad (2.34)$$

and

$$(G - B) / (R - B) > (0.5R - B) / (R - B) > 0.5 \quad (2.35)$$

$$(G - B) / (R - B) \leq (R - B) / (R - B) = 1 \quad (2.36)$$

The hue index H' is within the range $H' \in (0.5, 1]$, and the hue of pixel P can be determined correspondingly to be within the range of $(30^\circ, 60^\circ]$. According to [39], the saturation S and the value V can be calculated using

$$S = (C_{p,max} - C_{p,min}) / C_{p,max} = (R - B) / R \quad (2.37)$$

and

$$V = C_{p,max}/255 = R/255 \quad (2.38)$$

, where $R \in [0, 255]$ and $B \in [0, 255]$ are the R and B values of pixel P in the RGB color model. The ranges of the saturation and the value in the HSV model can be determined as $S \in [0, 1]$ and $V \in [0, 1]$, respectively, which implies all aforementioned light scenes are covered. According to Definition 3, this pixel can be classified as “yellow”. \square

Lemma 3. *The color of pixel P is “red” if and only if the C-R index ranges of the pixel satisfy $M \in [2, \infty)$, $N \in [0, 1]$, and $K \in [0, 1]$.*

Proof. Sufficient condition. According to Definition 4, the hue value is within the range of $H \in (0^\circ, 30^\circ]$. To cover all light scenes in Definition 1, $S \in [0, 1]$ and $V \in [0, 1]$. The R , G , and B values of pixel P in the RGB color model can be transformed from the HSV model using Eqs. (2.27)-(2.29). [36,37]

The color ratios M , N , and K of pixel P can be derived as shown in Eqs. (2.30)-(2.32). Since $H' \in (0, 0.5]$, $0.5 \leq |H' \bmod 2 - 1| < 1$. Additionally, because $S \in [0, 1]$, $0 \leq |H' \bmod 2 - 1| \leq 1$. Thus, the C-R indices are within the ranges of $M \in [1, \infty)$, $N \in [0, 1]$, and $K \in [0, 1]$. If $M \in [1, 2)$, according to Lemma 2, the color of the pixel P is “yellow”, thus the ranges of M , N , and K are redefined as $M \in [2, \infty)$, $N \in [0, 1]$, and $K \in [0, 1]$.

Necessary condition. According to Definition 5, if the C-R index ranges of pixel P are $M \in [2, \infty)$, $N \in [0, 1]$, and $K \in [0, 1]$, the R , G , and B values satisfy the relationships of $0 \leq B \leq G \leq R$ and $R \geq 2G$. The hue index H' can be calculated by Eq. (2.33) [39]. The maximum and minimum color components are $C_{p,max} = R$ and $C_{p,min} = B$, then $0 \leq G - B \leq R - B$.

According to Eq. (2.33),

$$0 \leq (G - B) / (R - B) \leq G/R \leq 0.5 \quad (2.39)$$

The hue index H' is within the range $H' \in (0, 0.5]$, and the hue of pixel P can be determined correspondingly to be within the range of $(0^\circ, 30^\circ]$. According to [39], the saturation S and the value V can be calculated using Eqs. (2.37) and (2.38). The ranges of the saturation and the value in the HSV model can be determined as $S \in [0, 1]$ and $V \in [0, 1]$, respectively, which implies all aforementioned light scenes are covered. According to Definition 4, this pixel can be classified as “red”. \square

Remark 1. *Three singularities need to be discussed. (1) If the R and G values of pixel P are zeros, the color of pixel P is considered as “blue”; (2) if the B and G values of pixel P are zeros, the color of pixel P is considered as “red”; and (3) if the R and B values of pixel P are zeros, the color of pixel P is considered as “green”.*

Simulation Validation of C-R Indices

There are a total of 16,777,216 colors in the 24-bit RGB color space. According to Definition 2, Definition 3, and Definition 5, there are 5,599,172, 1,404,903, and 1,384,405 of those colors are classified as “green”, “yellow”, and “red”, respectively. The performance of the color detection method is assessed by examining the ratios between color detections and the colors in their corresponding color categories. Five indices are adopted to evaluate the performance [40,41]: Accuracy (ACC), True Positive Rate (TPR), False Positive Rate (FPR), True Negative Rate (TNR), and False Negative Rate (FNR). ACC [41] describes the performance of correct detections, which is the ratio between the number of correctly detected colors and the total number of colors in the color base.

TPR [41] is the ratio between the number of correctly detected green/yellow colors and the total number of green/yellow colors, FPR [41] is the ratio between the number of falsely detected as the non-green/non-yellow colors and the total number of non-green/non-yellow colors, TNR [41] describes the ratio between the number of correctly detected non-green/non-yellow colors and the total number of non-green/non-yellow colors, and FNR [41] is the ratio between the number of falsely detected as green/yellow colors and the total number of green/yellow colors.

For the green color, the performance of the proposed color detection method is compared with an existing Green Leaf Index (GLI) [42] as

$$GLI = (2G - R - B) / (2G + R + B) \quad (2.40)$$

As shown in Table 2.1, all the greenness colors are successfully detected by both GLI and C-R indices, and TPRs for both methods are 100%. However, 24.81% extra colors which are not “green”, i.e. $FPR = 24.81\%$, are falsely detected by GLI. This number is much higher than that of the C-R indices, which is only 0.23%. The detection accuracy of C-R indices (ACC) reaches 99.84%, which is also much higher than that of GLI (83.47%).

As shown in Table 2.2, all the yellowness colors are successfully detected (TPR=100%) by the C-R indices method. The false detection rate is very low, i.e., $FPR=4.66\%$, and $ACC=95.73\%$ is high. In summary, the simulation result demonstrates that the proposed C-R indices can be used to detect the green and yellow colors in the color space, instead of using the hue values.

As shown in Table 2.3, all the reddish colors are successfully detected (TPR=100%) by the C-R indices method. The false detection rate is very low, i.e., $FPR=0.84\%$, and $ACC=99.29\%$ is very high. In summary, the simulation result demonstrates that the proposed C-R indices can be used to detect the green, yellow, and red colors in the color space, instead of using the hue values.

Table 2.1: Sensitivity and specificity analyses on the greenness detection

	TPR(%)	TNR(%)	FPR(%)	FNR(%)	ACC(%)
GLI	100	75.19	24.81	0	83.47
C-R	100	99.77	0.23	0	99.84

Table 2.2: Sensitivity and specificity analyses on the yellowness detection

	TPR(%)	TNR(%)	FPR(%)	FNR(%)	ACC(%)
C-R	100	95.34	4.66	0	95.73

Table 2.3: Sensitivity and specificity analyses on the reddish detection

	TPR(%)	TNR(%)	FPR(%)	FNR(%)	ACC(%)
C-R	100	95.34	4.66	0	95.73

CHAPTER 3: STRAWBERRY PLANT ALIVE STATUS DETECTION

This work appeared in [35], from Kong, X. and Xu, Y., Strawberry Plant Alive Status Detection and Relative Pixel Based Plant Localization, submitted to the ASME Journal of Dynamic System, Measurement, and Control in Jan, 2019.

Problem Definition

Plant alive status detection is the first step before conducting any inspections or rescues. The procedures of the operation are (1) The proposed color-ratio (C-R) indices are used to detect green and yellow pixels. (2) The centroids of the extracted leaves are then calculated and the Euclidean distance between the centroids are examined to group the leaves into plants. (3) The alive status of a plant is determined by its majority colors. The detection rate is expected to be higher than 98% under different light scenes.

Plant Alive Status Detection

In this section, the color-ratio (C-R) indices are introduced to detect green and yellow leaves from images. The centroids of extracted leaves are detected and grouped into plants. The plant alive status is then determined by the majority colors of its leaves.

Leaf Detection

The green and yellow leaves in an image are extracted by the aforementioned C-R indices. A median filter and morphology methods, such as dilations or erosions, are applied to improve the

extraction using the commands “*medfilt2*”, “*imdilate*”, and “*imerode*”, respectively, in MATLAB 2015b.

Plant Alive Status Detection

The extracted leaves are grouped into plants based on the distance between the centroids of two leaves. In this study, the centroids are detected using the MATLAB command “*centroids*”. Assuming that pixels $p(x_p, y_p)$ and $q(x_q, y_q)$ are the centroids of leaves p and q , respectively. The Euclidean distance $D(p, q)$ is [43]

$$D(p, q) = \|p - q\|_2 \quad (3.1)$$

If the distance $D(p, q)$ satisfies

$$D(p, q) \leq \ell \quad (3.2)$$

, p and q belong to the same plant, where $\ell \in \mathbb{R}$ is a threshold value and is determined experimentally. According to the growers, the plant alive status can be determined by the colors of its leaves, such that if the plant is alive, then it always has green leaves. If no green leaf exists, the plant is dead.

Experimental Validation

Strawberry Leaf Detection via C-R Indices

Figures 3.1-3.3 show the strawberry leaf detection performance in different light scenes using the proposed color detection method. Three different light scenes are considered: different times of

a day (Fig. 3.1), different weather (Fig. 3.2), and different growth stages (Fig. 3.3). It is worth mentioning that not all light scenes can possibly be included in the experiments and theoretically we have proven that these conditions are considered. The experiments show that the proposed color detection method can successfully detect the green and yellow leaves in all these light scenes.

Remark 2. *The ranges of C-R indices defined in Lemma 1 and Lemma 2 can detect the greenness and yellowness from the color base. However, practically some greenness or yellowness background noise are also detected. To remove the background noise, the ranges of C-R indices in the experiment are slightly adjusted to $M \in [0.6, 0.95]$, $N \in [0.1, 0.7]$, and $K \in [0, \infty)$ in detecting green leaves, and $M \in [1.05, 1.17]$, $N \in [0.5, 0.88]$, and $K \in [0.4, 0.75]$ in detecting yellow leaves.*

Plant Alive Status Detection

Thirty-four plants are captured by the video. According to the grower, the video includes twenty-seven alive plants and seven dead plants. The plant alive status detection method is applied, and the threshold value ℓ is chosen to be 80 pixels. All thirty-four plants are detected, and twenty-seven alive plants and seven dead plants are recognized, and the success rate is 100%.

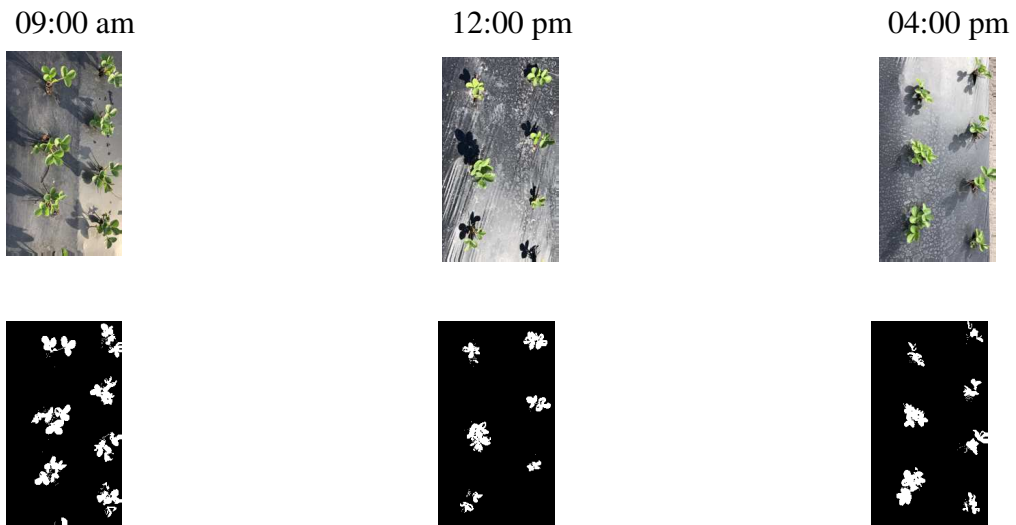


Figure 3.1: Leaf detection using the C-R indices in different times of a day (The pictures are captured from the Pappy's Patch, Orlando, FL, on Nov. 3rd, 2018)

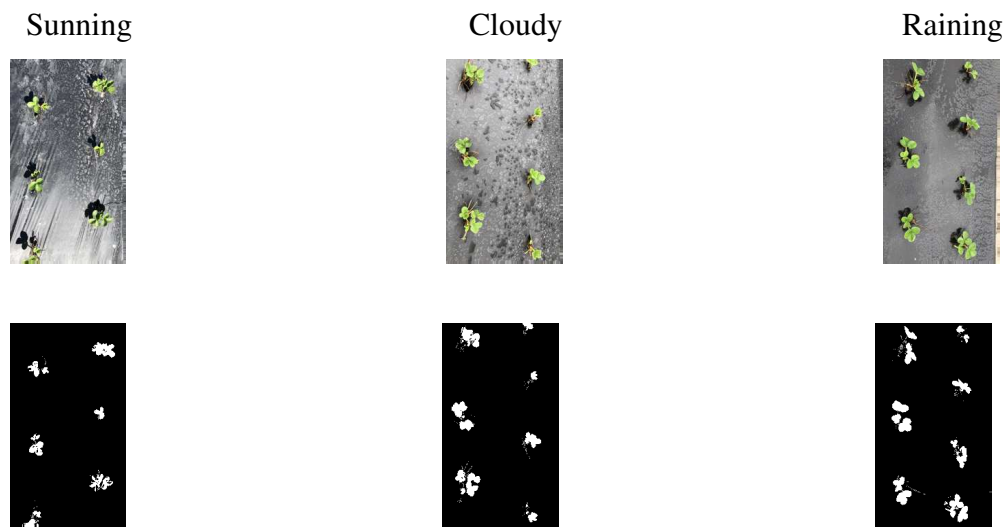


Figure 3.2: Leaf detection using the C-R indices in different weather conditions (The images are captured from the Pappy's Patch, Orlando, FL, on Oct. 30th, 2018, Oct. 23th, 2018, and Oct. 26th, 2018, respectively)

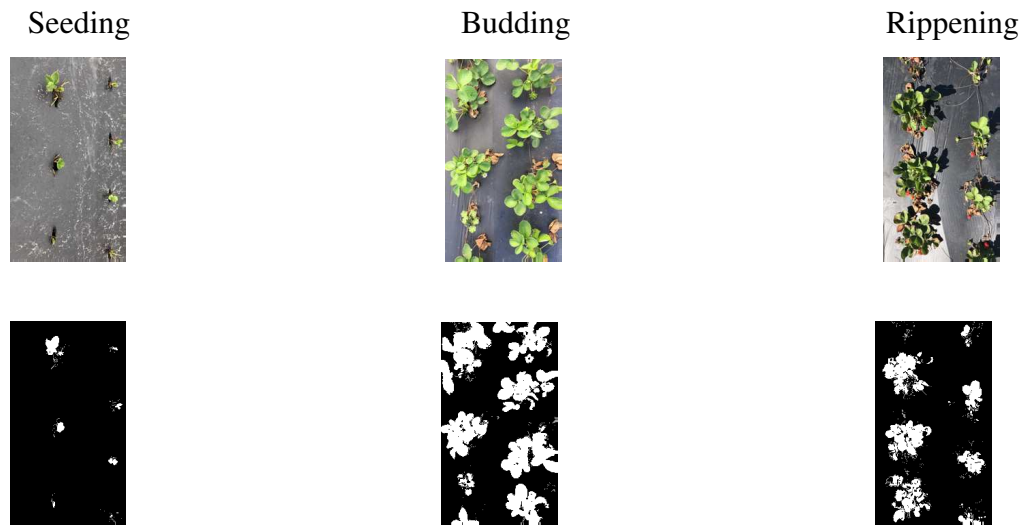


Figure 3.3: Leaf detection using the C-R indices in different growing stages (The images are captured from the Pappy's Patch, Orlando, FL, on Nov. 3rd, 2018, Dec. 1st, 2017, and Mar. 12th, 2018, respectively)

CHAPTER 4: STRAWBERRY PLANT LOCALIZATION VIA RELATIVE PIXEL

This work appeared in [35], from Kong, X. and Xu, Y., Strawberry Plant Alive Status Detection and Relative Pixel Based Plant Localization, submitted to the ASME Journal of Dynamic System, Measurement, and Control in Jan, 2019.

Problem Definition

The procedure of this operation is shown in Fig. 4.1. First, the proposed color-ratio (C-R) indices are used to detect the plant alive status as discussed in CHAPTER 3. After that, the relative pixel positions of adjacent plants are measured using the plant centroids, and an EKF is designed to estimate the relative positions between adjacent plants, as well as the absolute positions of them. The objective of the plant localization problem is that The plant localization error should be in the centimeter level.

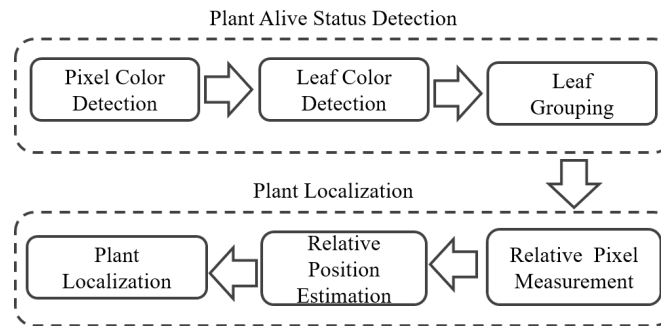


Figure 4.1: The procedure of plant alive status detection and localization

Plant Localization via Relative Pixel Position

Here, a new plant localization approach is proposed using the relative pixel information. The process model and the measurement model are developed, and a continuous extended Kalman filter (EKF) is designed to estimate the relative and absolute positions of plants.

Process Model

The state variables are chosen to be [44]

$$\mathbf{x} = [x_r, y_r, \varphi, x_1, y_1, x_2, y_2]^T \quad (4.1)$$

, in which x_r and y_r are the field robot position components in the robot body frame Ω_R , φ is the heading angle of field robot, and $[x_i, y_i], i = 1, 2$ is the position of the i^{th} plant in the inertia frame Ω_I . The process model is [44, 45]

$$\mathbf{f}(\mathbf{x}, \mathbf{u}, \mathbf{w}, t) = B\mathbf{u} + \mathbf{w} \quad (4.2)$$

, where $\mathbf{u} = [v, \omega]^T$, in which v represents the speed of robot, and ω is the angular velocity, respectively. $\mathbf{w} \in \Re^{7 \times 1}$ is a Gaussian noise, and $B \in \Re^{7 \times 2}$ is defined as [44, 45]

$$B = \begin{bmatrix} \cos \varphi & \sin \varphi & 0 & 0 & 0 & 0 & 0 \\ 0 & 0 & 1 & 0 & 0 & 0 & 0 \end{bmatrix}^T \quad (4.3)$$

Measurement Model

As shown in Fig. 4.2, the posture of the field robot is defined by its position (x_I, y_I, z_I) in the inertia frame Ω_I and the heading angle φ . The origin point O_r of the robot body frame Ω_R is chosen to be the mass center of robot. Two cameras are mounted on the inside-top of the field robot with a pitch angle ϕ as shown in Fig. 4.2. The camera frame $\Omega_C (x_c, y_c, z_c)$ is placed on the cameras.

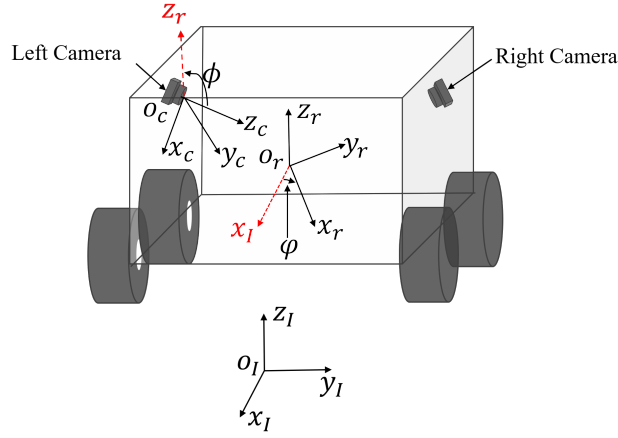


Figure 4.2: The coordinates of the field robot

Assume that there is a camera on the field robot with the position of $\mathbf{x}_c^{(R)} = [b_x, b_y, b_z]^T$ in Ω_R . Then the position of the camera in Ω_I can be given as

$$\mathbf{x}_c^{(I)} = \mathbf{x}_r^{(I)} + R^{(I/R)} \mathbf{x}_c^{(R)} \quad (4.4)$$

, where $\mathbf{x}_c^{(I)} = [x_c, y_c, z_c]^T$ and $\mathbf{x}_r^{(I)} = [x_r, y_r, z_r]^T$ are the positions of camera and field robot in Ω_I , respectively. $R^{(I/R)} \in \mathbb{R}^{3 \times 3}$ is the rotation matrix from Ω_R to Ω_I .

The relative position $\boldsymbol{\rho}_{c/P_i}^{(I)} \in \mathbb{R}^{3 \times 1}$ of a plant P_i to the camera in Ω_I is

$$\boldsymbol{\rho}_{c/P_i}^{(I)} = \mathbf{x}_{P_i}^{(I)} - \mathbf{x}_c^{(I)} \quad (4.5)$$

, where $\mathbf{x}_{P_i}^{(I)} = [x_{p,i}, y_{p,i}, z_{p,i}]^T$ is the position of plant P_i in Ω_I . The relative position $\boldsymbol{\rho}_{c/P_i}^{(I)}$ in Eq. (4.5) can be transferred to be in Ω_C using

$$\boldsymbol{\rho}_{c/P_i}^{(C)} = R^{(C/I)} \boldsymbol{\rho}_{c/P_i}^{(I)} \quad (4.6)$$

, where $\boldsymbol{\rho}_{c/P_i}^{(C)} = [\rho_{x,i}^{(C)}, \rho_{y,i}^{(C)}, \rho_{z,i}^{(C)}]^T$ and $R^{(C/I)} \in \mathbb{R}^{3 \times 3}$ is the rotation matrix from Ω_I to Ω_C . The pixel position of plant P_i can be expressed as

$$\mathbf{x}_{P_i}^{(P)} = \left(K_c / \rho_{z,i}^{(C)} \right) \boldsymbol{\rho}_{c/P_i}^{(C)} \quad (4.7)$$

, where $K_c \in \mathbb{R}^{2 \times 3}$ is the intrinsic matrix as

$$K_c = \begin{bmatrix} f_x & 0 & c_x \\ 0 & f_y & c_y \end{bmatrix} \quad (4.8)$$

, where $[f_x, f_y]$ and $[c_x, c_y]$ are the focal length and the principle point of camera, respectively.

Assuming that there are adjacent plants P_1 and P_2 in the field, the position of the adjacent plants in Ω_I are $\mathbf{x}_{P_1}^{(I)}$ and $\mathbf{x}_{P_2}^{(I)}$, respectively. The pixel positions of P_1 and P_2 in the image can be expressed according to Eq. (4.7) as

$$\mathbf{x}_{P_1}^{(P)} = \left(K_c / \rho_{z,1}^{(C)} \right) \boldsymbol{\rho}_{c/P_1}^{(C)} \quad (4.9)$$

and

$$\mathbf{x}_{P_2}^{(P)} = \left(K_c / \rho_{z,2}^{(C)} \right) \boldsymbol{\rho}_{c/P_2}^{(C)} \quad (4.10)$$

The relative pixel position $\boldsymbol{\rho}_{P_1/P_2}^{(P)} \in \Re^{3 \times 1}$ between P_1 and P_2 is then calculated using

$$\boldsymbol{\rho}_{P_1/P_2}^{(P)} = K_c \left(\boldsymbol{\rho}_{c/P_2}^{(C)} / \rho_{z,2}^{(C)} - \boldsymbol{\rho}_{c/P_1}^{(C)} / \rho_{z,1}^{(C)} \right) \quad (4.11)$$

The relative pixel position $\boldsymbol{\rho}_{P_1/P_2}^{(P)}$ in Eq. (4.11) can be expanded as

$$\boldsymbol{\rho}_{P_1/P_2}^{(P)} = \begin{bmatrix} p_{x,1} - p_{x,2} \\ p_{y,2} - p_{y,1} \end{bmatrix} \quad (4.12)$$

, where

$$p_{x,1} = \frac{f_x (x'_1 \cos \phi + b_x + y'_1 \sin \phi)}{z'_1 \cos \phi - b_y \sin \phi - x'_1 \sin \phi \sin \phi + y'_1 \sin \phi \cos \phi} \quad (4.13)$$

$$p_{x,2} = \frac{f_x (x'_2 \cos \phi + b_x + y'_2 \sin \phi)}{z'_2 \cos \phi - b_y \sin \phi - x'_2 \sin \phi \sin \phi + y'_2 \sin \phi \cos \phi} \quad (4.14)$$

$$p_{y,1} = \frac{f_y (z'_1 \sin \phi - b_y \cos \phi + x'_1 \cos \phi \sin \phi - y'_1 \cos \phi \cos \phi)}{z'_1 \cos \phi - b_y \sin \phi - x'_1 \sin \phi \sin \phi + y'_1 \sin \phi \cos \phi} \quad (4.15)$$

and

$$p_{y,2} = \frac{f_y (z'_2 \sin \phi - b_y \cos \phi + x'_2 \cos \phi \sin \phi - y'_2 \cos \phi \cos \phi)}{z'_2 \cos \phi - b_y \sin \phi - x'_2 \sin \phi \sin \phi + y'_2 \sin \phi \cos \phi} \quad (4.16)$$

, in which

$$x'_1 = x_{p,1} - x_r, \quad x'_2 = x_{p,2} - x_r \quad (4.17)$$

$$y'_1 = y_{p,1} - y_r, \quad y'_2 = y_{p,2} - y_r \quad (4.18)$$

and

$$z'_1 = b_z - z_{p,1} + z_r, \quad z'_2 = b_z - z_{p,2} + z_r \quad (4.19)$$

Assumption 2. *The robot scouts along a horizontal plane with a constant speed. The position component z_r of the field robot in Ω_R is considered as a constant, such that $z_r = h_r$.*

Assumption 3. *The plants are planted on a horizontal plane. The position components $z_{p,i}$ of plants in Ω_I are considered as constants, such that $z_{p,i} = h_p$.*

Depending on the motion of the field robot and the distribution of crops, there are three special cases discussed here.

Case 1: If the planting beds have straight-line edges, and the robot travels straight forward with a constant heading angle $\varphi = 0^\circ$, the relative pixel position in Eqs. (4.13-4.16) can be simplified as

$$p_{x,1} = [f_x (x'_1 + b_x)] / (z'_1 \cos \phi - b_y \sin \phi + y'_1 \sin \phi) \quad (4.20)$$

$$p_{x,2} = f_x (x'_2 + b_x) / (z'_2 \cos \phi - b_y \sin \phi + y'_2 \sin \phi) \quad (4.21)$$

$$p_{y,1} = \frac{f_y (z'_1 \sin \phi - b_y \cos \phi - y'_1 \cos \phi)}{z'_1 \cos \phi - b_y \sin \phi + y'_1 \sin \phi} \quad (4.22)$$

and

$$p_{y,2} = \frac{f_y (z'_2 \sin \phi - b_y \cos \phi - y'_2 \cos \phi)}{z'_2 \cos \phi - b_y \sin \phi + y'_2 \sin \phi} \quad (4.23)$$

Case 2: If the plants are aligned well, and the positions of plants in the y -direction are constants, such that $y'_1 = y'_2 = c$, the relative pixel position in Eqs. (4.13-4.16) can be simplified as

$$p_{x,1} = \frac{f_x (x'_1 \cos \varphi + b_x + c \sin \varphi)}{z'_1 \cos \phi - b_y \sin \phi - x'_1 \sin \phi \sin \varphi + c \sin \phi \cos \varphi} \quad (4.24)$$

$$p_{x,2} = \frac{f_x (x'_2 \cos \phi + b_x + c \sin \phi)}{z'_2 \cos \phi - b_y \sin \phi - x'_2 \sin \phi \sin \phi + c \sin \phi \cos \phi} \quad (4.25)$$

$$p_{y,1} = \frac{f_y (z'_1 \sin \phi - b_y \cos \phi + x'_1 \cos \phi \sin \phi - c \cos \phi \cos \phi)}{z'_1 \cos \phi - b_y \sin \phi - x'_1 \sin \phi \sin \phi + c \sin \phi \cos \phi} \quad (4.26)$$

and

$$p_{y,2} = \frac{f_y (z'_2 \sin \phi - b_y \cos \phi + x'_2 \cos \phi \sin \phi - c \cos \phi \cos \phi)}{z'_2 \cos \phi - b_y \sin \phi - x'_2 \sin \phi \sin \phi + c \sin \phi \cos \phi} \quad (4.27)$$

Case 3: If the plants are aligned well on a straight-line edge planting bed, and the heading angle of the field robot and the position components of plants in the y -direction are constants, such that $\phi = 0^\circ$ and $y'_1 = y'_2 = c$, the relative pixel position in Eqs. (4.13-4.16) can be simplified as

$$p_{x,1} = [f_x (x'_1 + b_x)] / (z'_1 \cos \phi - b_y \sin \phi + c \sin \phi) \quad (4.28)$$

$$p_{x,2} = f_x (x'_2 + b_x) / (z'_2 \cos \phi - b_y \sin \phi + c \sin \phi) \quad (4.29)$$

$$p_{y,1} = \frac{f_y [z'_1 \sin \phi - (b_y + c) \cos \phi]}{z'_1 \cos \phi + (c - b_y) \sin \phi} \quad (4.30)$$

and

$$p_{y,2} = \frac{f_y [z'_2 \sin \phi - (b_y + c) \cos \phi]}{z'_2 \cos \phi + (c - b_y) \sin \phi} \quad (4.31)$$

According to Assumption 2 and Assumption 3, z'_1 and z'_2 in Eq. (4.19) are $z'_1 = z'_2 = b_z - h_p + h_r$,

thus the relative pixel position of adjacent plants in Eq. (4.12) can be simplified as

$$\boldsymbol{\rho}_{P_1/P_2}^{(P)} = \begin{bmatrix} m(x_2 - x_1) \\ 0 \end{bmatrix} \quad (4.32)$$

, where

$$m = f_x / [z \cos \phi + (c - b_y) \sin \phi] \quad (4.33)$$

The measurements obtained from the images are the relative pixel positions of adjacent plants as

$$\mathbf{y} = [\rho_{rel,x}^{(P)}, \rho_{rel,y}^{(P)}]^T \quad (4.34)$$

, where $\rho_{rel,x}^{(P)}$ and $\rho_{rel,y}^{(P)}$ are the relative pixel position components along the x and y directions, respectively. The measurement model is defined as

$$\mathbf{h}(\mathbf{x}, \mathbf{v}, t) = \boldsymbol{\rho}_{P_1/P_2}^{(P)} + \mathbf{v} \quad (4.35)$$

, where $\boldsymbol{\rho}_{P_1/P_2}^{(P)}$ is the relative pixel position derived in Eq. (4.12), and $\mathbf{v} \in \Re^{2 \times 1}$ is a zero mean Gaussian noise with a covariance matrix of R .

Extended Kalman Filter

The detailed steps for developing the EKF are following [46–48]. The partial derivative matrices at the current state estimate are

$$A = \partial \mathbf{f} / \partial \mathbf{x} |_{\hat{\mathbf{x}}} \quad (4.36)$$

$$L = \partial \mathbf{f} / \partial \mathbf{w} |_{\hat{\mathbf{x}}} \quad (4.37)$$

$$\tilde{C} = \partial \mathbf{h} / \partial \mathbf{x} |_{\hat{\mathbf{x}}} \quad (4.38)$$

and

$$\tilde{M} = \partial \mathbf{h} / \partial \mathbf{v} |_{\hat{\mathbf{x}}} \quad (4.39)$$

, where $\hat{\mathbf{x}}$ is the state estimate, \mathbf{f} is the process function in Eq. (4.2), and \mathbf{h} is the measurement function in Eq. (4.35), respectively.

Remark 3. *The experiments were conducted in a commercial strawberry farm, of which the planting beds do not have straight line edges and some plants are not perfectly aligned. Therefore, the partial derivatives in Eq. (4.36) through Eq. (4.39) are derived based on the general equations in Eqs. (4.12-4.19), as shown in Appendix A.*

The update equation of state covariance matrix \tilde{P} is

$$\tilde{P} = A\tilde{P} + \tilde{P}A^T + \tilde{Q} - \tilde{P}\tilde{C}^T\tilde{R}^{-1}\tilde{C}\tilde{P} \quad (4.40)$$

, where \tilde{Q} and \tilde{R} are defined as

$$\tilde{Q} = LQL^T \quad (4.41)$$

and

$$\tilde{R} = \tilde{M}R\tilde{M}^T \quad (4.42)$$

The Kalman gain is calculated by

$$\tilde{K} = \tilde{P}\tilde{C}^T\tilde{R}^{-1} \quad (4.43)$$

The state estimate $\hat{\mathbf{x}}$ is updated using

$$\dot{\hat{\mathbf{x}}} = \mathbf{f}(\hat{\mathbf{x}}, \mathbf{u}, \mathbf{w}_0, t) + \tilde{K}(\mathbf{y} - \mathbf{h}(\hat{\mathbf{x}}, \hat{\mathbf{v}}_0, t)) \quad (4.44)$$

, where \mathbf{w}_0 and \mathbf{v}_0 are the zero nominal noise values.

The absolute positions of the plants are determined by the estimate relative positions of adjacent plants. The first plant of the detected rows is selected as the origin point of Ω_I .

Experiment Validation and Discussions

Experiment Settings

The experiments of plant alive status detection and localization are conducted with a custom designed differential-drive ground robot in a commercial strawberry farm as shown in Fig. 4.3. The robot specifications can be found in [45, 49]. The robot moves about 10m along the strawberry bed with a constant speed of 0.23 m/s, covering thirty-four strawberry plants. The first plant is set as the origin point of Ω_I . We use a tape to measure the true values of the relative and absolute positions of plants. A digital camera with a resolution of 1280x720 pixels captures videos at 30 fps. The images are then rescaled to be 600x338 pixels using the command “*imresize*” in MATLAB 2015b to reduce the computational cost. All the images are processed offline at 5 fps, and the actual size of each pixel square is about 0.16x0.16 cm².



Figure 4.3: The ground robot in a strawberry farm

Plant Localization Validation

In the last step of plant localization experiment, the measurement inputs of relative pixel positions of adjacent plants are calculated using the difference between the centroids. A linear interpolation technique is applied to increase the data points among all the images. P_0 , Q , and R in Eqs. (4.40-4.43) are tuned to be

$$P_0 = \text{diag} \{ [0.01 \ 0.01 \ 0.01 \ 0.01 \ 0.01 \ 35 \ 35] \} \quad (4.45)$$

$$Q = \text{diag} \{ [0.1 \ 0.1 \ 0.1 \ 0.1 \ 0.1 \ 10 \ 10] \} \quad (4.46)$$

and

$$R = \text{diag} \{[10 \ 10]\} \quad (4.47)$$

The measured and estimated relative positions are shown in Fig. 4.4, in which the estimated relative positions in the x and y directions follow the measurements. The mean errors are 2.24 cm in the x direction and 0.49 cm in the y direction, respectively, as shown in Fig. 4.5.

The measured and estimated absolute positions of plants are shown in Fig. 9. The estimated positions of the strawberry plants follow the measured positions. The errors in the x and y directions are cumulative errors as shown in Fig. 10. The mean errors are 3.06 cm in the x direction and 0.51 cm in the y direction, respectively, which meet the centimeter level accuracy requirement.

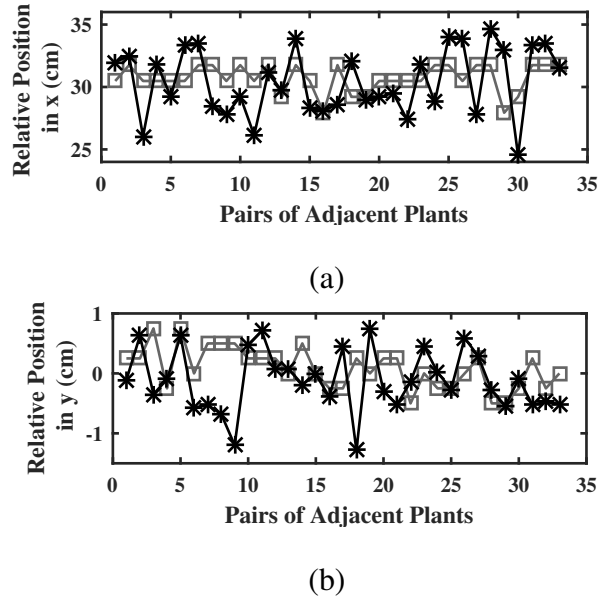
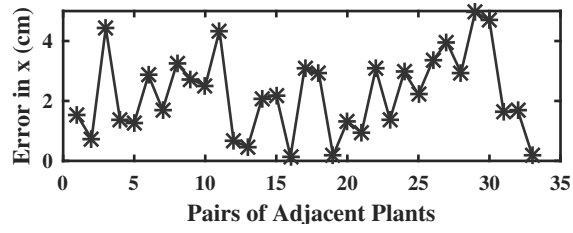
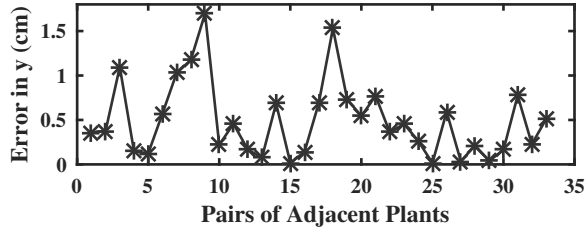


Figure 4.4: The measured and estimated relative positions of adjacent plants. (a) Relative positions in the x direction, and (b) relative position in the y direction. The squared line and the starred line represent the measurements and the estimates, respectively



(a)



(b)

Figure 4.5: The errors between the measured and estimated relative positions. (a) The error in the x direction, and (b) the error in the y direction

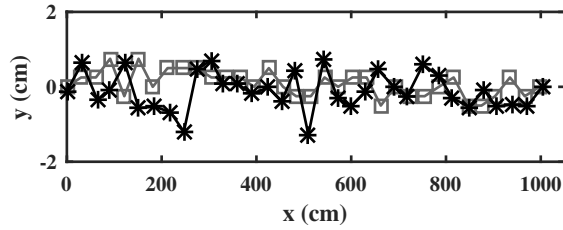
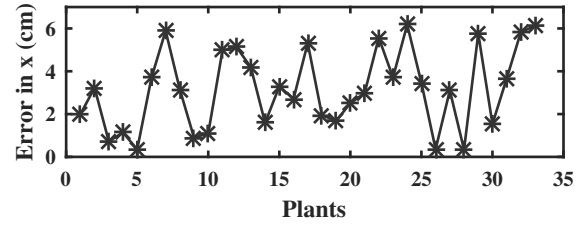
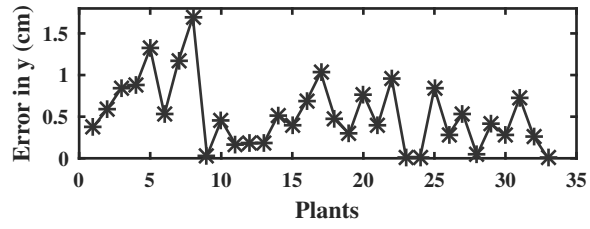


Figure 4.6: The measured and estimated absolute positions of the strawberry plants in the field. The squared line and the starred line represent the measurements and the estimates, respectively



(a)



(b)

Figure 4.7: The errors of the measured and estimated absolute positions. (a) The error in the x direction, and (b) the error in the y direction

CHAPTER 5: Strawberry Plant Nutrient Deficiency Detection

For strawberry crops, deficiencies in nitrogen (N), phosphorus (P), and potassium (K) are prevalent. Figure 5.1 presents some strawberry leaf images when the crops are healthy or are experiencing the N, P, and K deficiencies. For example, when the crop suffers the K-deficiency, scorch color appears along the edge of leaflets as shown in Fig. 5.1 (b). If the crop is experiencing the N-deficiency, the color of leaflet alters from healthy green (i.e., Fig. 5.1 (a)) to yellow-green (i.e., Fig. 5.1 (d)). If the crop is under the P-deficiency, some purple colors are expected as shown in Fig. 5.1(c). Thus, such observable color features and their distribution patterns can be used to detect or predict possible nutrient deficiencies. It is worth noting that sometimes crops could suffer multiple nutrient deficiencies (i.e., Fig. 5.1(e) and (f)).



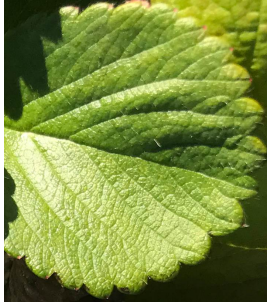
(a) Healthy leaf



(b) K deficiency



(c) P deficiency



(d) N deficiency



(e) N and K deficiencies



(f) N, P, and K deficiencies

Figure 5.1: Deficiencies on strawberry leaf. (a)-(c) are provided by Dr. Shinsuke Agehara from the University of Florida, and (d)-(f) are captured from the Pappy's Patch in Orlando, FL and labeled by Dr. Shinsuke Agehara from the University of Florida

Problem Definition

There are two steps involved in the proposed nutrient deficiency detection method. As shown in Fig. 5.2, in Step 1, the target strawberry leaflet is segmented using the Sobel operator [50] and morphology techniques [11] from leaf image. The deficiency color is recognized by the C-R indices and its pattern is calculated using the method we discuss next. In Step 2, the color and pattern information is used to determine the possible nutrient deficiencies. The pattern recognition accuracy of the deficiency of strawberry leaflet is expected to achieve 95%, and the nutrient deficiency detection should approach the human-level inspection level.

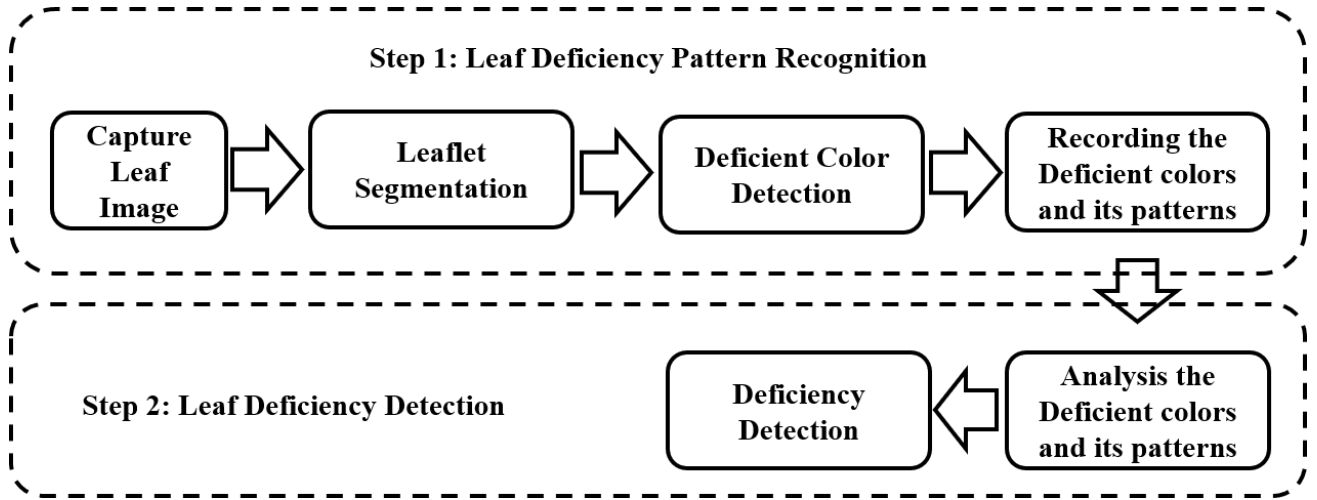


Figure 5.2: The procedure of the proposed nutrient deficiency detection method

Nutrient Deficiency Detection

The colors and their distribution patterns on a plant leaf are the main characters to identify the deficiencies. According to [34], ten out of thirteen strawberry plant deficiencies can be identified only by its color and color distribution pattern, and the other 3 deficiencies can be identified by the shape of those leaves.

Leaf Segmentation with Sobel Operator

In fields, leaves are interlaced among each other. It is necessary to segment the target leaflet before conducting the deficiency detection. In this study, a bilateral filter is used first to reduce the image noise [51]. Different from using a Gaussian filter [52], the bilateral filter not only can reduce the noise, but also can better preserve edge information.

The Sobel operator is a first derivative edge detection algorithm [53], which includes two 3x3 kernels as shown in Fig. 5.3. Comparing with the other operators, such as the 2^{nd} order Laplace or the Robert operators [54,55], it has relatively smaller kernels and is less sensitive to the noise.

-1	-2	-1
0	0	0
1	2	1

-1	0	1
-2	0	2
-1	0	1

Figure 5.3: The 3x3 kernels of Sobel operator. The images are cited from [11,53]

The edges in the image are detected by calculating the gradient as [53]

$$g(i, j) = \sqrt{S_x^2 + S_y^2} \quad (5.1)$$

, where S_x and S_y represent the partial derivatives of pixel P in the x and y directions and are defined as [50,56]

$$S_x = \{f(i+1, j-1) + 2f(i+1, j) + f(i+1, j+1)\} \\ - \{f(i-1, j-1) + 2f(i-1, j) + f(i-1, j+1)\} \quad (5.2)$$

and

$$S_y = \{f(i-1, j+1) + 2f(i, j+1) + f(i+1, j+1)\} \\ - \{f(i-1, j-1) + 2f(i, j-1) + f(i+1, j-1)\} \quad (5.3)$$

, where $f(i, j)$ is the gray scale value of a pixel $P(i, j)$.

A sensitivity threshold value k is introduced to extract the edges, such that if

$$g(i, j) \geq k \quad (5.4)$$

Then the pixel $P(i, j)$ is the edge. Here, $k = 0.07$.

The leaf segmentation is processed in MATLAB R2018b. To strengthen the segmentation, a median filter and the morphology operations, such as dilation and erosion, are applied by using the commands “medfilt2”, “imerode”, and “imdilate”. The center point of the leaflet is then determined by the command “regionprops”.

Nutrient Deficiency Symptom Pattern Recognition

The nutrient deficiency symptom pattern recognition includes two parts: nutrient deficiency color feature extraction and distribution pattern examination.

Nutrient Deficiency Color Feature Recognition

The C-R indices are used to extract the color features of the leaves with nutrient deficiencies. As shown in Table 1.1, the strawberry leaflet turns yellow-green, purple, or scorch when it is experiencing nitrogen, phosphorus, or potassium deficiencies, respectively. According to a plant

scientist the purple and scorch colors in strawberry plants are the red color with different shades. In this study, the red color discussed in Section 2 is divided into two color categories: scorch and purple. To define the purple and scorch colors of strawberry plants, 3775 scorch pixels and 35313 purple pixels are collected from the field images. As shown in Fig. 5.4, the distributions of the C-R indices N and K of the scorch and purple colors have similar distributions, while the index M implies a different distribution between the scorch and purple colors. Further, the distributions of the values of R , G , and B are analyzed. As shown in Fig. 5.5, the values of R of the scorch and purple are distinct: the mean values of R of the purple and scorch colors are 227 and 128, respectively. Therefore, a threshold can be set to distinguish the scorch and purple colors as in Definition 6.

Definition 6. *If the color of pixel P is identified as “red” according to Lemma 3, and the value of R is less than 130, then the color of P is defined as “scorch”. Otherwise the “red” pixel P is defined as “purple”.*

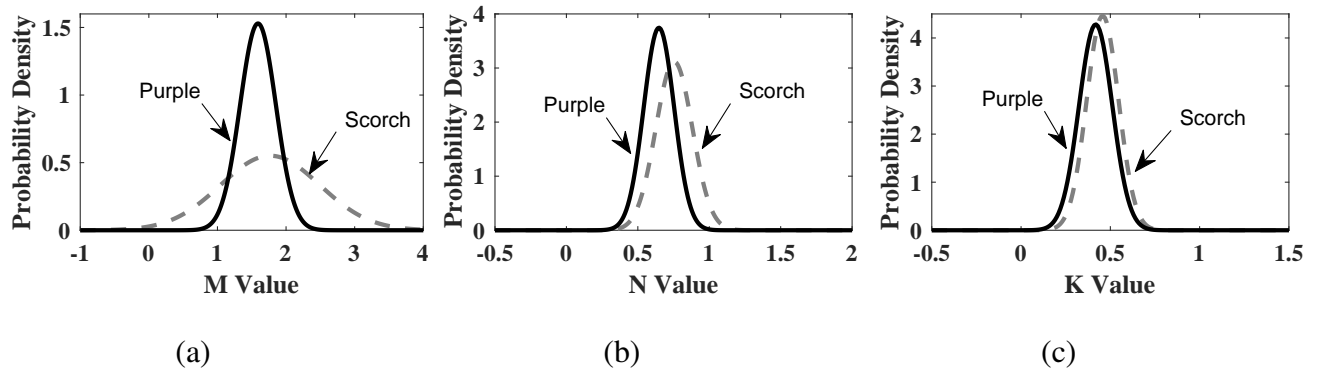


Figure 5.4: The C-R indices of the scorch and purple pixels of strawberry deficiency: (a) the M index, (b) the N index, and (c) the K index.

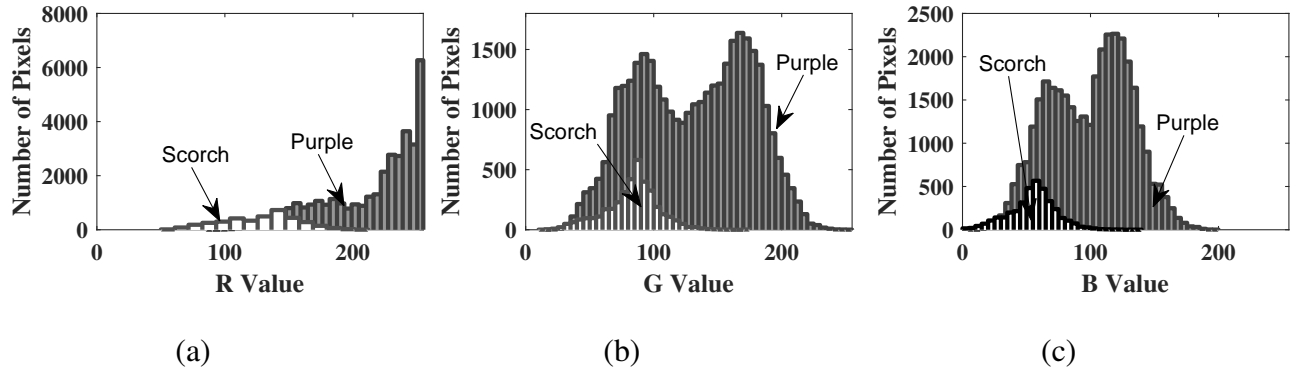


Figure 5.5: The R , G , and B values of the scorch and purple pixels of strawberry deficiency: (a) the R value, (b) the G value, and (c) the B value.

In Chapter 2, Lemma 1 introduced and proven the ranges of C-R indices for detecting the green pixels. In the nutrient deficiency detection, the green colors defined in Definition 2 need to be divided into two independent green color sets: the healthy green and the yellow-green, in which the healthy green color describes a green pixel presented in healthy leaves, while the yellow-green color describes a green pixel suffers N-deficiency. To investigate the differences of the C-R index ranges between the healthy green color and the yellow-green color, Fig. 5.6 analyzes 3395 healthy green colors and 26640 yellow-green colors collected from the strawberry leaf images. As shown in Fig. 5.6, the C-R indices M , N and K of the healthy green and yellow-green colors are distinct. Therefore, the C-R indices ranges for detecting the yellow-green colors can be adjusted experimentally as $M \in [0.8, 1.025]$, $N \in (0.4, 0.57)$, and $K \in (0.4, 0.7)$, while the C-R indices ranges of $M \in [0.5, 0.7]$, $N \in (0.6, 1]$, and $K \in (1.1, \infty)$ can be used to detect the healthy green color.

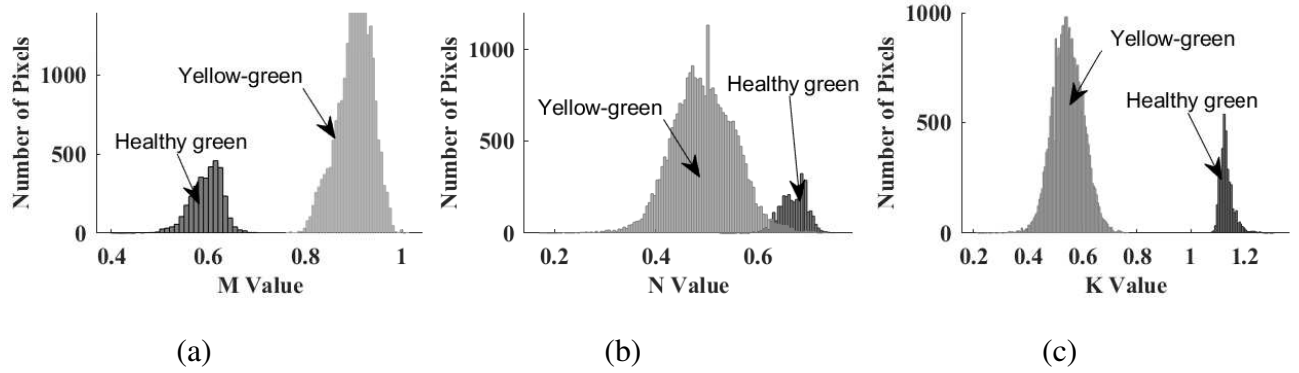


Figure 5.6: The C-R indices of the healthy green and yellow-green pixels of strawberry leaves: (a) the M index, (b) the N index, and (c) the K index.

Color Distribution Pattern Recognition

The color distribution pattern recognition is to identify the location and pattern of those deficiency colors on a strawberry leaflet. In plant science, the inspection regions of a leaflet can be divided into three areas: marginal, sub-marginal, and internal. As shown in Fig. 5.7, the marginal area is defined as the contour of a leaflet. The centers of the detected color regions are determined. The distance $\mathbf{l} = [l_1, l_2, \dots, l_k]^T$ between the center point O of the leaflet to the centroids O_k of the k^{th} detected color regions is measured as

$$l_k(O, O_k) = \|O - O_k\|_2 \quad (5.5)$$

The internal area is then defined as an enclosed circle with a radius of r , which is defined as

$$r = \frac{1}{3} \max_{i \in [1, k]} l_i \quad (5.6)$$

The sub-marginal is the area between the marginal and the internal areas.

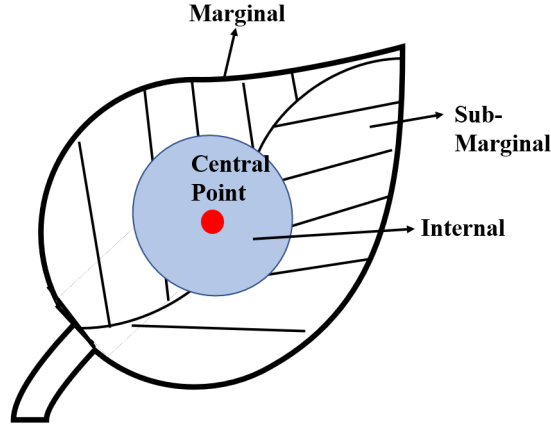


Figure 5.7: The definition of the distribution area of nutrient deficiency

Nutrient Deficiency Detection via Leaf Feature Extraction

The procedures of the nutrient deficiency detection approach are: (1) the target leaflet is segmented from an uncertain background by using the Sobel operator and morphology techniques, (2) the deficiency patterns of the leaflet are recognized with the C-R indices. (3) The deficiencies are determined with the information of the extraceted leaf features. [34]. It is worth noting that only the nitrogen, phosphorus, and potassium of the strawberry are studies here.

Fig. 5.8 shows an example of how to apply the proposed nutrient deficiency detection approach on a strawberry leaflet. Fig. 5.8 (a) is a leaflet image collected from a commercial strawberry farm. The Sobel operator and the morphology techniques are applied to segment the leaflet from the surroundings as shown in Fig. 5.8 (b). The marginal area is the area along the contour of the leaflet. The center point O of the leaflet is then determined and marked as the red point in Fig. 5.8

(c). Sixty-four deficient regions of this leaflet are detected and the centroids O_k , $k = 1, \dots, 64$ of the detected deficient regions are marks as green points in Fig. 5.8 (c). The distances between the leaflet center O to the centroids O_k are examined, where the maximum distance and the minimum distance are 714.18 pixels and 151.67 pixels, respectively. According to Eq. (5.6), the radius of the circle for determining the internal area is

$$r = \frac{1}{3} \max_{i \in [1, 64]} l_i = 238.06 \text{ pixels} \quad (5.7)$$

Then the internal area of the leaflet is determined by a circle area with the radius of r as shown in Fig. 5.8 (c). The sub-marginal area is the area between the marginal and the internal areas.

The proposed C-R indices ranges are used to extract the nutrient deficiency colors features. The detected nutrient deficiency colors and distributions are shown in Fig. 5.8 (c). Table 5.1 analyzes the results of the inspection. The nutrient deficiency color includes the yellow-green, purple, and scorch, which are represented by the colors green, purple, and brown in Fig. 5.8 (c), respectively. The inspection region includes the marginal, sub-marginal, and internal areas which have been properly determined. The binary value (1 or 0) in the Table 5.1 indicates if the nutrient deficiency color appears in that inspection region. The nutrient deficiency are detect by the extracted color features and distribution patterns. According to the [34], the leaflet in Fig. 5.8 (a) suffers nitrogen, phosphorus, and potassium deficiencies.

Table 5.1: Nutrient deficiency color and color distribution pattern inspection by using the C-R indices

Inspection Region	Nutrient Deficiency Colors		
	Yellow-green	Purple	Scorch
Marginal	1	1	1
Sub-marginal	1	1	1
Internal	1	1	0

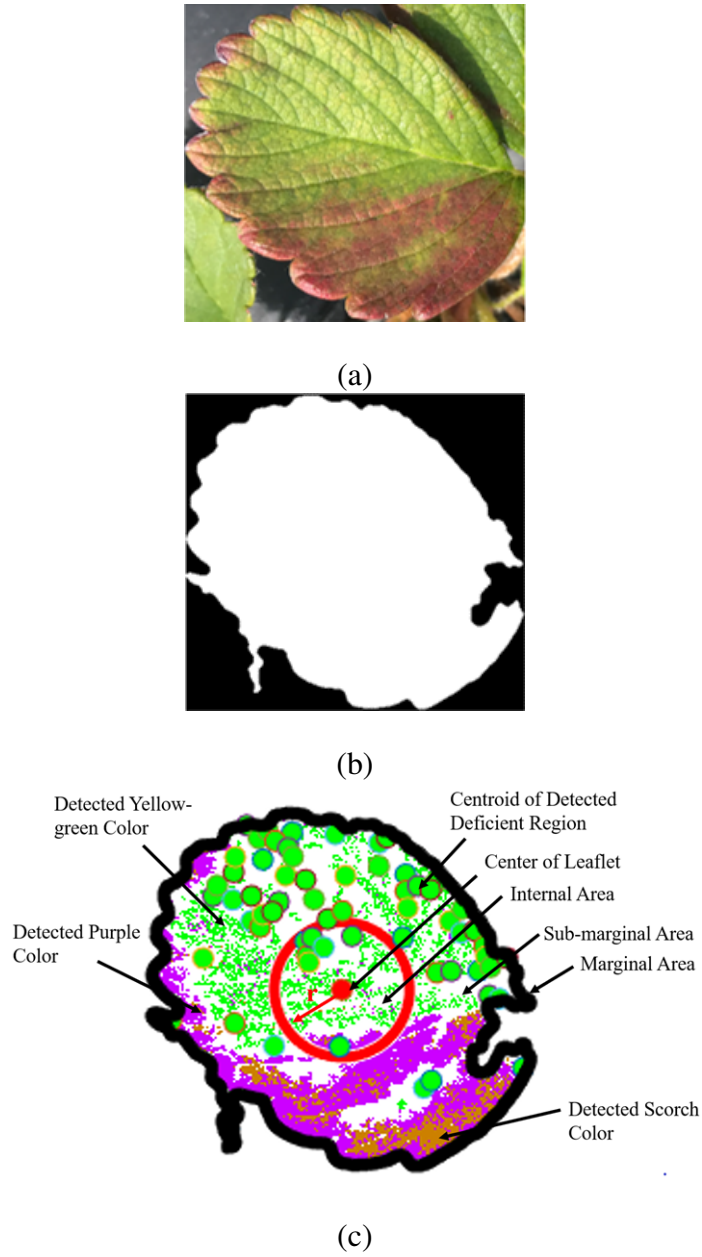


Figure 5.8: Strawberry plant nutrient deficiency detection using the proposed approach. (a) A leaflet in the field, (b) the segmented leaf using the Sobel operator, and (c) the characterized colors and their locations. The image is captured from Pappy's Patch on Feb. 23, 2019.

Experimental Validation

Experiment Setting

The proposed nutrition deficiency detection algorithm is validated with a total of 110 strawberry leaflet images in the experiment. The images are collected with an Apple iPhone X from a local commercial strawberry farm in Orlando, Florida. The resolution of the images is 1226x1343 pixels. The detection algorithm is programmed and operated in Matlab 2018b with a 2.50GHz Intel(R) Core(TM) i7-6500U CPU, 12 GB RAM, and 64-bit Windows 10 Home operating system. The leaflets are labeled by a plant scientist from the University of Florida to validate the performance of the nutrition deficiency detection approach.

Nutrient Deficiency Symptom Pattern Recognition

The leaflets are segmented from natural field backgrounds by using the Sobel operator and morphology techniques. The feature extraction method is applied on each image by examining the nutrient deficiency colors and its patterns. The result shows that all deficiency patterns are correctly recognized, and the success rate achieves 100%.

Nutrient Deficiency Detection via Leaf Feature Extraction

The leaflet features are extracted by using the proposed C-R indices. The average process time is 1.41 s. Three statistics indices are applied to evaluate the performance of the deficiency detection approach: precision, recall, and accuracy, which are defined as follows [57].

$$precision = \frac{\# True Positive}{\# True Positive + \# False Positive} \quad (5.8)$$

$$recall = \frac{\# True Positive}{\# True Positive + \# False Negative} \quad (5.9)$$

and

$$recall = \frac{\# Correctly \ detected \ deficiencies}{The \ total \ number \ of \ the \ leaflets} \quad (5.10)$$

, where the true positive is defined as the total number of the detection approach correctly points out labeled deficiencies, the false positive is the total number of the detection approach falsely points out the deficiencies, and the false negative is the detection approach fails to point out the labeled deficiencies. As shown in Table 5.2, the precision and recall are high, and the accuracy rate achieves 96.36%. Thus, we can argue that the proposed nutrition deficiency detection method via image leaf feature extraction can achieve the human-level inspection.

Table 5.2: Performance of the nutrition deficiency detection approach in strawberry leaflets

Index	Precision(%)	Recall(%)	Accuracy(%)
Result	97.24	99.07	96.36

CHAPTER 6: IMPROVED CONTROL AFFINE, APPROXIMATED WHEEL TERRAIN INTERACTION MODEL FOR A GROUND SCOUTING ROBOT

This work appeared in [58], from Menendez-Aponte, P., Kong, X. and Xu, Y., An Approximated, Control Affine Model for a Strawberry Field Scouting Robot Considering WheelTerrain Interaction, Robotica, March, 2019.

The approximated, control affine wheel Terrain interaction model (WTIM) for a ground scouting robot was initially done by Pablo Menendez-Aponte in his Master thesis [59]. The longitudinal and the lateral forces were approximated by an exponential function of the slip ratio and a linear function of slip angle. However, the huge errors (around 40%) between the approximated model and the experimental data can not meet the requirements. In this chapter, an improved approximated WTIM model is proposed. Different from [59], the longitudinal force is curve-fitted using a polynomial function of the slip ratio, while the lateral force is curve-fitted using an exponential function of both the slip ratio and slip angle. It is worth noting that the derivations of the kinematic model of the skid steer, the dynamic model of the field robot, and the EKF are omitted in this chapter. Those derivations can be found in [59].

Terramechanics WTIM Simulation

The derived WTIM is simulated for single-wheel, linear motion. The simulation results are used to analyze the relationships among slip/skid ratio, slip angle, longitudinal force, and lateral force. The parameters related to off-road soils are taken from [60]. The longitudinal and lateral forces are evaluated as the slip ratio varies from -0.5 to 0.5 and the slip angle varies from 0° to 16°

following [60,61].

As shown in Fig. 6.1, the longitudinal force $F_{w,x}$ varies significantly with respect to the slip ratio λ due to the changing shear deformation; while it maintains relatively stationary when the slip angle β changes. It can be seen in Fig. 6.2 that the lateral force $F_{w,y}$ depends not only on λ but also on β . It is worth noting that the simulation results achieved here match well with the results shown in [61].

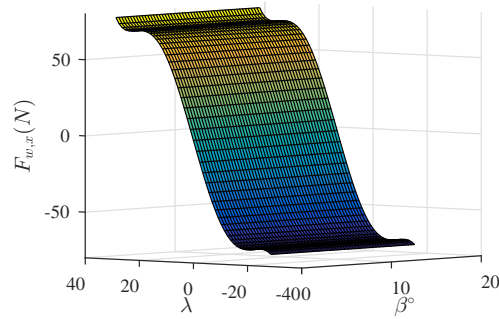


Figure 6.1: Longitudinal reaction force simulated using the full WTIM with a torus shape.

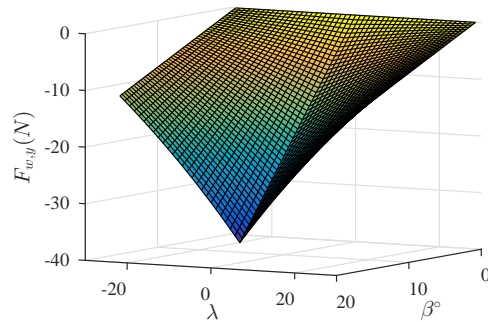


Figure 6.2: Lateral reaction force simulated using the full WTIM with a torus shape.

Approximated Wheel Terrain Interaction Model

While the terramechanic model shown in Section 3.1 allows for accurate simulation and analysis of the wheel-terrain interaction forces in soft terrain, it does not have a control affine format [62–64] and thus is not convenient for guidance, navigation, and control design. Also, the full WTIM is computationally expensive. A large body of research has shown that λ and β are two critical elements in off-road wheel-terrain interactions [60, 61, 63–69]. Based on Fig. 6.1, a polynomial function is used to approximate the longitudinal force $F_{w,x}$ as

$$F_{w,x} = \sum_{i=0}^k c_i \lambda^i \quad (6.1)$$

, where $c_i, i = 0, 1, \dots, k$ are the parameters of the polynomial function.

Observing the trend of lateral force in Fig. 6.2, $F_{w,y}$ decreases when the slip ratio λ increases and increases along β increases. Thus we approximate $F_{w,y}$ as

$$F_{w,y} = -d_1 \beta (d_2 + e^{-d_3 \lambda}) \quad (6.2)$$

, where d_1, d_2 and d_3 are the parameters to be identified.

Two criteria are used to quantify the performance of the approximation: the mean absolute error (MAE) and the R-square value. In Table I, it can be seen that the 4th order polynomials MAE value is the lowest, while the R-square value increases as the order of the polynomial fit increases. However, it is worth mentioning that a higher order polynomial will have higher computational costs and will introduce more parameters which must be identified. Therefore, a 4th order polynomial was chosen to approximate the longitudinal force in this study. Table II lists the performance of the approximation for the lateral force. Here, the MAE values are below 0.15 while the R-square

values are all above 0.99 for each slip angle case. Thus, we can argue that the approximated WTIM longitudinal force and lateral force can be used when controlling the field robot. Any approximation errors can be handled by a well-tuned robust or adaptive controller. It is worth noting that the parameters obtained offline via the least squares approach can be used as initial guesses; the actual values can vary with terrain conditions, and should be identified online via the extended Kalman Filter (EKF), discussed in a later section.

Table 6.1: Goodness of fit for the longitudinal force in the approximated WTIM

Slip angle Polynomial		$\beta = 4^\circ$	$\beta = 8^\circ$	$\beta = 12^\circ$	$\beta = 16^\circ$
3^{rd} order	MAE	0.7366	0.6491	0.5311	0.4204
	R-square	0.9887	0.9923	0.9956	0.9977
4^{th} order	MAE	0.5110	0.4433	0.3672	0.3174
	R-square	0.9955	0.9970	0.9982	0.9989
5^{th} order	MAE	0.1575	0.1379	0.1452	0.1709
	R-square	0.9994	0.9995	0.9996	0.9996
6^{th} order	MAE	0.1267	0.1394	0.1526	0.1748
	R-square	0.9996	0.9996	0.9996	0.9996

Table 6.2: Goodness of fit for the lateral force in the approximated WTIM

Slip angle Evaluation	$\beta = 4^\circ$	$\beta = 8^\circ$	$\beta = 12^\circ$	$\beta = 16^\circ$
MAE	0.0213	0.0351	0.0585	0.1254
R-square	0.9999	0.9999	0.9998	0.9996

Approximated Control Affine Model

The nonlinear control affine model is following the form presented in [59] as

$$\dot{x} = f(x) + g(x)u \quad (6.3)$$

, where $\mathbf{x} \in \Re^{11 \times 1}$, $\mathbf{u} \in \Re^{2 \times 1}$ are the state vector and control variables presented in [59]. $\mathbf{f}(\mathbf{x}) \in \Re^{11 \times 1}$, and $\mathbf{g}(\mathbf{x}) \in \Re^{11 \times 2}$ are the state function and control input matrix, which are defined as

$$\mathbf{f}(\mathbf{x}) = \begin{bmatrix} \dot{\psi}_R \dot{y}_R + 2 \left[\sum_{i=0}^k c_i (\lambda_r^k + \lambda_l^k) \right] / m \\ -\dot{\psi}_R \dot{x}_R - d_1 [k_r (\beta_1 + \beta_3) + k_l (\beta_2 + \beta_4)] / m \\ \left\{ 2W \sum_{i=0}^k c_i (\lambda_l^k - \lambda_r^k) + d_1 L [k_r (\beta_3 - \beta_1) + k_l (\beta_4 - \beta_2)] \right\} / I \\ -k_\omega \omega_r \\ -k_\omega \omega_l \\ f_{\lambda,r} \\ f_{\lambda,l} \\ (\dot{x}_1 \ddot{y}_1 - \dot{y}_1 \ddot{x}_1) / (\dot{y}_1^2 + \dot{x}_1^2) \\ (\dot{x}_2 \ddot{y}_2 - \dot{y}_2 \ddot{x}_2) / (\dot{y}_2^2 + \dot{x}_2^2) \\ (\dot{x}_3 \ddot{y}_3 - \dot{y}_3 \ddot{x}_3) / (\dot{y}_3^2 + \dot{x}_3^2) \\ (\dot{x}_4 \ddot{y}_4 - \dot{y}_4 \ddot{x}_4) / (\dot{y}_4^2 + \dot{x}_4^2) \end{bmatrix} \quad (6.4)$$

and

$$\mathbf{g}(\mathbf{x}) = \begin{bmatrix} 0 & 0 & 0 & k_\omega & 0 & g_{\lambda,r} & 0 & 0 & 0 & 0 & 0 \\ 0 & 0 & 0 & 0 & k_\omega & 0 & g_{\lambda,l} & 0 & 0 & 0 & 0 \end{bmatrix}^T \quad (6.5)$$

In the obtained control-affine approximated model, the unknown parameters $c_i, i = 0, \dots, 4$, and $d_i, i = 1, 2, 3$ will be estimated via an EKF.

States and Unknown Parameters Estimation

Directly measuring the unknown parameters $c_i, i = 0, 1, 2, 3, 4$ and $d_i, i = 1, 2, 3$ in the derived model is challenging. Furthermore, these parameters vary with different terrains, such as loamy

soils and sandy soils. To tackle these issues, a hybrid EKF is developed to estimate the unknown parameters of the proposed approximated WTIM, such that the propagated state variables can match experimental data.

The state variables and the unknown parameters to be simultaneously estimated are

$$\mathbf{x}_{ext} = \left[\dot{x}_R, \dot{y}_R, \dot{\psi}_R, \omega_r, \omega_l, c_0, c_1, c_2, c_3, c_4, d_1, d_2, d_3 \right]^T \quad (6.6)$$

The measurements are presented in [59]. The process model and the measurement model can be expressed, respectively, as

$$\mathbf{f}_{ext}(\mathbf{x}_{ext}, \mathbf{u}, \mathbf{w}) = \begin{bmatrix} \dot{\psi}_R \dot{y}_R + 2 \left[\sum_{i=0}^k c_i (\lambda_r^k + \lambda_l^k) \right] / m \\ \ddot{y}_R \\ \ddot{\psi}_R \\ -k_\omega \omega_r \\ -k_\omega \omega_l \\ 0 \\ 0 \\ 0 \\ 0 \\ 0 \\ 0 \\ 0 \\ 0 \\ 0 \end{bmatrix} + \begin{bmatrix} \mathbf{w}_1 \\ \mathbf{w}_2 \\ \mathbf{w}_3 \\ \mathbf{w}_4 \\ \mathbf{w}_5 \\ \mathbf{w}_6 \\ \mathbf{w}_7 \\ \mathbf{w}_8 \\ \mathbf{w}_9 \\ \mathbf{w}_{10} \\ \mathbf{w}_{11} \\ \mathbf{w}_{12} \\ \mathbf{w}_{13} \end{bmatrix} \quad (6.7)$$

and

$$\mathbf{h}(\mathbf{x}_{ext}, \mathbf{v}) = \begin{bmatrix} \dot{\psi}_R \dot{y}_R + 2 \left[\sum_{i=0}^k c_i (\lambda_r^k + \lambda_l^k) \right] / m \\ -\dot{\psi}_R \dot{x}_R - d_1 [k_r (\beta_1 + \beta_3) + k_l (\beta_2 + \beta_4)] / m \\ \dot{\psi}_R \\ \omega_r \\ \omega_l \end{bmatrix} + \begin{bmatrix} \mathbf{v}_1 \\ \mathbf{v}_2 \\ \mathbf{v}_3 \\ \mathbf{v}_4 \\ \mathbf{v}_5 \end{bmatrix} \quad (6.8)$$

, where $\mathbf{w} = [\mathbf{w}_i]_{i=1, \dots, 13}$ and $\mathbf{v} = [\mathbf{v}_i]_{i=1, \dots, 5}$ are assumed to be zero mean white Gaussian noises with covariances of \mathbf{Q} and \mathbf{R} , respectively. The detailed steps in designing the hybrid EKF can be found in [46].

Experiment Validation

A scouting experiment is conducted to validate the EKF algorithm in estimating the state variables and the unknown parameters of the approximated, control affine model. Here, the Disease Detection Agricultural Ground Robot (“DDAGR”), shown in Fig. 5, is used as the robot platform, and is commanded to cover three strawberry rows in a commercial farm. Afterwards, the EKF is run off-line using the data acquired in the experiment.



Figure 6.3: DDAGR in front of a strawberry bed in a commercial strawberry orchard.

Experiment Validation

The experiment is conducted in a sandy loam commercial strawberry farm. The strawberry bed size is about $1m$ and the spacing between beds is roughly $0.5m$. The scouting path consists of two phases as shown in Fig. 6.4. Phase 1 is referred to as the over-bed motion. Here, the robot scouts over the bed along the bed centerline with a constant speed. Phase 2 is referred to as the cross-bed motion, which is further separated as three sections. First, a 90° in-site rotation is taken after the robot passes the headland of the current row (Phase 2.1). Second, a translation allows DDAGR to move towards the next row (Phase 2.2). Finally, another 90° in-site rotation makes the robot align with the next row (Phase 2.3). A PID controller and a sliding mode controller are applied to the over-bed motion and the cross-bed motion, respectively [45]. The wheel angular velocities are varied at the time instances as listed in Table 6.3 with a time step of $\Delta t = 0.13s$.

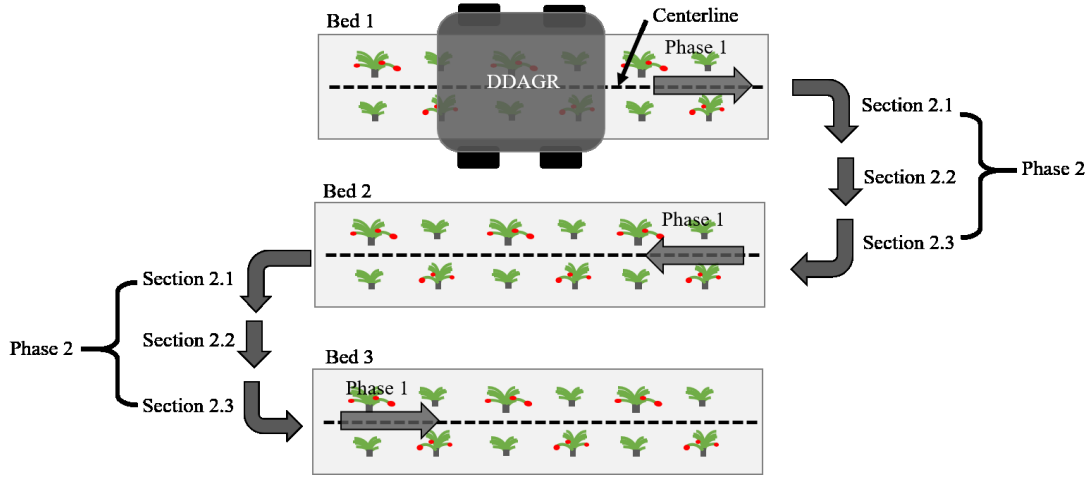


Figure 6.4: A scouting path covering three rows in a commercial strawberry farm.

The initial error covariance matrix P_0 , the process covariance matrix Q , and the measurement covariance matrix R used in the experiment, respectively, are

$$P_0 = \text{diag}\{[0.01 \ 0.01 \ 1 \ 0.002 \ 0.002 \ 10 \ 10 \ 10 \ 10 \ 10 \ 10 \ 10 \ 10]\} \quad (6.9)$$

$$Q = \left\{ \begin{array}{l} \text{diag} \{ [10 \ 10 \ 600000 \ 100 \ 100 \ 1 \ 1 \ 1 \ 1 \ 1 \ 1 \ 1] \times 10^{-5} \}, 0s \leq t < 118.69s \\ \text{diag} \{ [60000 \ 15000 \ 200000 \ 100 \ 100 \ 1 \ 1 \ 1 \ 1 \ 1 \ 1 \ 1] \times 10^{-5} \}, 118.69s \leq t < 134.16s \\ \text{diag} \{ [40000 \ 10000 \ 10000 \ 10000 \ 10000 \ 1 \ 1 \ 1 \ 1 \ 1 \ 1 \ 1] \times 10^{-5} \}, 134.16s \leq t < 142.35s \\ \text{diag} \{ [40000 \ 40000 \ 250000 \ 10000 \ 10000 \ 1 \ 1 \ 1 \ 1 \ 1 \ 1 \ 1] \times 10^{-5} \}, 142.35s \leq t < 157.3s \\ \text{diag} \{ [40 \ 10 \ 2000 \ 10000 \ 10000 \ 1 \ 1 \ 1 \ 1 \ 1 \ 1 \ 1] \times 10^{-5} \}, 157.3s \leq t < 762.58s \\ \text{diag} \{ [60000 \ 15000 \ 500000 \ 1000 \ 1000 \ 1 \ 1 \ 1 \ 1 \ 1 \ 1 \ 1] \times 10^{-5} \}, 762.58s \leq t < 777.66s \\ \text{diag} \{ [40000 \ 20000 \ 250000 \ 10000 \ 10000 \ 1 \ 1 \ 1 \ 1 \ 1 \ 1 \ 1] \times 10^{-5} \}, 777.66s \leq t < 785.33s \\ \text{diag} \{ [40000 \ 20000 \ 20000 \ 10000 \ 10000 \ 1 \ 1 \ 1 \ 1 \ 1 \ 1 \ 1] \times 10^{-5} \}, 785.33s \leq t < 800.41s \\ \text{diag} \{ [20 \ 1 \ 200 \ 10000 \ 10000 \ 1 \ 1 \ 1 \ 1 \ 1 \ 1 \ 1] \times 10^{-5} \}, 800.41s \leq t < 918.19s \end{array} \right. \quad (6.10)$$

and

$$R = \text{diag} \{ [0.015 \ 0.1 \ 0.015 \ 10^{-5} \ 10^{-5}] \} \quad (6.11)$$

Table 6.3: Wheel bank velocities used in the scouting motion experiment

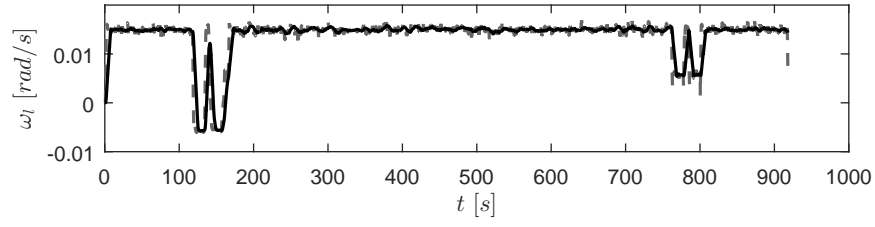
$t (s)$	$\omega_r (rad/s)$	$\omega_l (rad/s)$
0.00 – 118.69	0.82	0.82
118.69 – 134.16	0.32	−0.32
134.16 – 142.35	0.82	0.82
142.35 – 157.30	0.32	−0.32
157.30 – 762.58	0.82	0.82
762.58 – 777.66	−0.32	0.32
777.66 – 785.33	0.82	0.82
785.33 – 800.41	−0.32	0.32
800.41 – 918.19	0.82	0.82

The estimated wheel angular velocities are shown in Fig. 6.5. It can be seen that the estimated angular velocities track the measurements and match the commands listed in Table 6.3. Figure 6.6 shows the measured and estimated longitudinal velocity \dot{x}_R , lateral velocity \dot{y}_R , and yaw rate $\dot{\psi}_R$, respectively. The results indicate that DDAGR starts with an over-bed motion scouting over the first strawberry bed with a longitudinal velocity about $0.23m/s$. At about $120s$, it turns and starts moving towards the second bed. The turning yaw rate is about $0.15rad/s$, and the translation is with a longitudinal velocity around $0.23m/s$, respectively. Beginning at $160s$, DDAGR scouts over the second bed with a constant longitudinal velocity of $0.23m/s$. Once it reaches the headland of the second bed at around $790s$, a cross-bed motion with a yaw rate of $0.15rad/s$ and a longitudinal velocity of $0.23m/s$ allows the robot to move towards the third strawberry bed. From $800s$ to $920s$, the robot scouts the third strawberry bed with a longitudinal velocity of $0.23m/s$. The trace value of the error covariance matrix is shown in Fig. 6.7, indicating that the EKF is stable and works

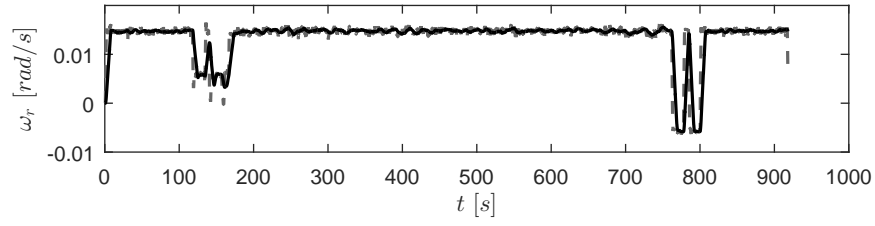
properly.

Figure 6.8 shows the estimated scouting motion trajectory. The estimated trajectory is obtained by integrating the estimated velocities. Referring to Fig. 6.6, DDAGR moves forward along the centerline of the first bed with a longitudinal velocity of $0.23m/s$. After traveling about $30m$, it reaches the headland of the first bed. The robot moves from the first bed to the second bed between $120s$ and $160s$, then starts scouting over the second bed for about $130m$. DDAGR moves towards the third bed from $760s$ to $800s$, scouts $40m$ in the third bed, then stops.

Figure 6.9 shows the estimates of unknown parameters of the approximated WTIM $\hat{c}_i, i = 0, 1, 2, 3, 4$ and $\hat{d}_i, i = 1, 2, 3$. Due to varying terrain and motion conditions, the estimated parameters are stabilized at different values for different sections and phases. However all these estimated parameters vary within a small range. Therefore, it is not a challenging task to design a proper controller that is robust or adaptive with respect to such parametric uncertainties.

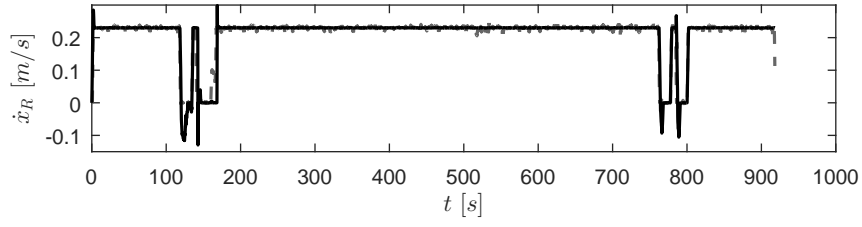


(a)

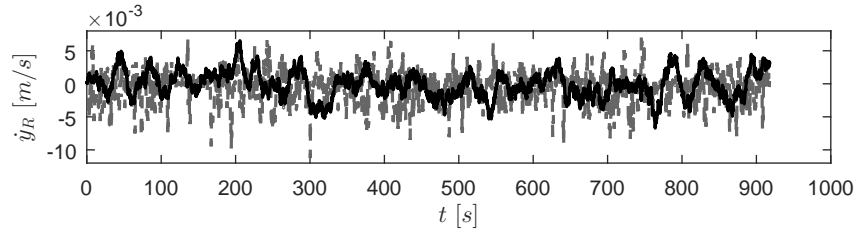


(b)

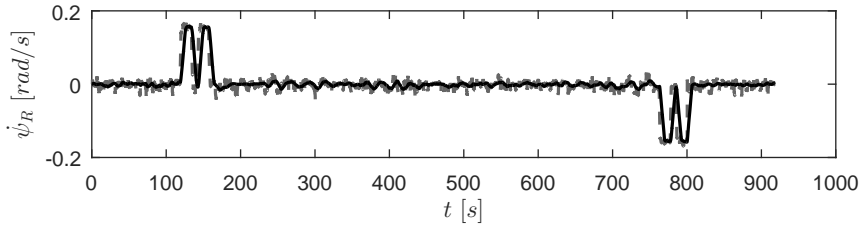
Figure 6.5: Measured and estimated wheel velocities of DDAGR in the scouting motion: (a) left wheel angular velocity and (b) right wheel angular velocity. The dotted and solid lines represent the measurement and estimation, respectively.



(a)



(b)



(c)

Figure 6.6: Measured and estimated velocities of DDAGR in the scouting motion: (a) longitudinal velocity, (b) lateral velocity, and (c) yaw rate, where the dotted and solid lines represent the measurement and estimation, respectively.

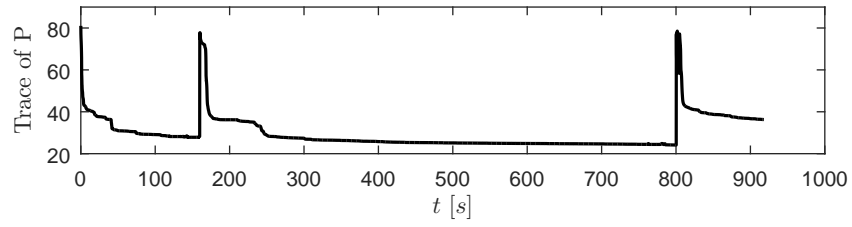


Figure 6.7: Trace of the error covariance matrix of DDAGR in the scouting motion.

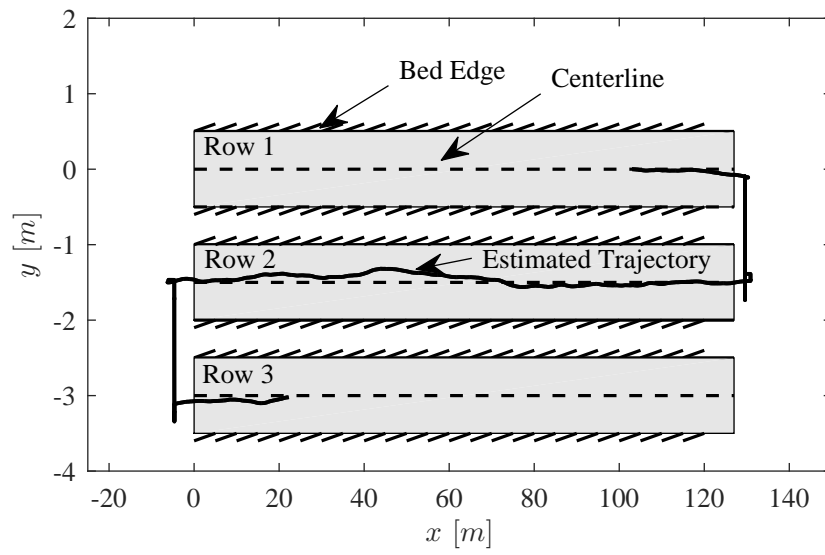


Figure 6.8: The estimated trajectory of DDAGR in the scouting motion.

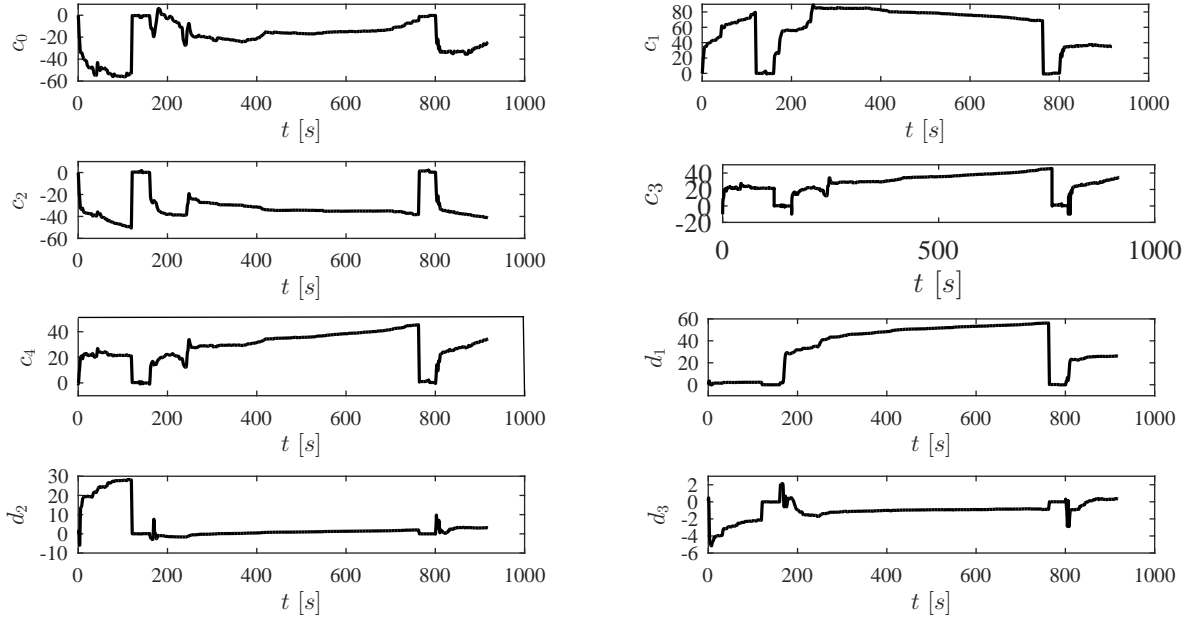


Figure 6.9: Parameter estimation of DDAGR approximated WTIM in the scouting motion: \hat{c}_0 , \hat{c}_1 , \hat{c}_2 , \hat{c}_3 , and \hat{c}_4 are the parameters in the longitudinal force model; while \hat{d}_1 , \hat{d}_2 , and \hat{d}_3 are the parameters in the lateral force model.

CHAPTER 7: CONCLUSION AND FUTURE WORK

Conclusions

In Chapter 2, the new color-ratio (C-R) index is proposed to detect green, yellow, and red colors. The simulations manifest that the proposed C-R indices can be used to detect the green, yellow, and red colors in the color space, instead of using the hue values.

In Chapter 3, a new plant alive status detection method by using the C-R indices is proposed. The proposed method is successfully validated in a commercial strawberry farm. 100% of the plants are successfully detected and all 27 alive plants and 7 dead plants are correctly recognized. The C-R indices method is proven to be robust with respect to varying light conditions (e.g., different time of a day, different weather conditions, and different growing stages).

In Chapter 4, a differential style approach is developed for plant localization by using the relative pixel positions of adjacent plants. An extended Kalman filter is developed to estimate both the relative and absolute positions of plants. A centimeter level estimate accuracy is achieved by the low cost and lightweight plant localization method.

In Chapter 5, an image-based low-cost plant nutrient deficiency detection method is proposed. The experiment validates that 100% of the leaflets are successfully recognized and 96.3% deficiencies are detected which match the human-level inspections.

Future Work

The color-ratio (C-R) indices presented in Chapter 2 currently only considered the colors of red, yellow, and green. A complete C-R ranges for other colors, such as violet, blue, orange, etc., should be investigated.

The nutrient deficiency detection method presented in Chapter 5 only focuses on nitrogen (N), phosphorus (P), and potassium (K) deficiencies. More deficiencies could be considered in the future. Besides, more experiments could be conducted to verify the performance of the proposed method with different conditions, which include but not limit to different farms, different weather, different growing stages. Finally, the chemical test of strawberry leaflet could be applied to validate the accuracy of the deficiency detection method.

We have utilized the relationships between location and color of the leaflet image and nutrient deficiency. They can regarded as input and output, respectively, in deep learning (e.g. neural network). Therefore, one future task will be using deeping learning methods to enhance the accuracy of the nutrient deficiency detection.

APPENDIX A: PARTIAL DERIVATIVE MATRICES OF RELATIVE PIXEL POSITION IN THE EKF

A brief derivation of the partial derivative matrices in Eqs. (4.36-4.39) is shown in this section.

According to Eq. (4.1) and Eq. (4.12), the partial derivative matrices can be derived as

$$\begin{aligned}
 A &= \partial \mathbf{f} / \partial \mathbf{x} |_{\hat{\mathbf{x}}} \\
 &= \begin{bmatrix} 0 & 0 & -\sin \varphi & 0 & 0 & 0 & 0 \\ 0 & 0 & \cos \varphi & 0 & 0 & 0 & 0 \\ 0 & 0 & 0 & 0 & 0 & 0 & 0 \\ 0 & 0 & 0 & 0 & 0 & 0 & 0 \\ 0 & 0 & 0 & 0 & 0 & 0 & 0 \\ 0 & 0 & 0 & 0 & 0 & 0 & 0 \\ 0 & 0 & 0 & 0 & 0 & 0 & 0 \end{bmatrix}_{\hat{\mathbf{x}}} \quad (A.1)
 \end{aligned}$$

$$L = \partial \mathbf{f} / \partial \mathbf{w} |_{\hat{\mathbf{x}}} = \text{diag} \{[1, 1, 1, 1, 1, 1, 1]\} \quad (A.2)$$

$$\begin{aligned}
 \tilde{C} &= \partial \mathbf{h} / \partial \mathbf{x} |_{\hat{\mathbf{x}}} \\
 &= \begin{bmatrix} \partial p_{x,1} / \partial x_r - \partial p_{x,2} / \partial x_r & \partial p_{y,2} / \partial x_r - \partial p_{y,1} / \partial x_r \\ \partial p_{x,1} / \partial y_r - \partial p_{x,2} / \partial y_r & \partial p_{y,2} / \partial y_r - \partial p_{y,1} / \partial y_r \\ \partial p_{x,1} / \partial \varphi - \partial p_{x,2} / \partial \varphi & \partial p_{y,2} / \partial \varphi - \partial p_{y,1} / \partial \varphi \\ \partial p_{x,1} / \partial x_1 - \partial p_{x,2} / \partial x_1 & \partial p_{y,2} / \partial x_1 - \partial p_{y,1} / \partial x_1 \\ \partial p_{x,1} / \partial y_1 - \partial p_{x,2} / \partial y_1 & \partial p_{y,2} / \partial y_1 - \partial p_{y,1} / \partial y_1 \\ \partial p_{x,1} / \partial x_2 - \partial p_{x,2} / \partial x_2 & \partial p_{y,2} / \partial x_2 - \partial p_{y,1} / \partial x_2 \\ \partial p_{x,1} / \partial y_2 - \partial p_{x,2} / \partial y_2 & \partial p_{y,2} / \partial y_2 - \partial p_{y,1} / \partial y_2 \end{bmatrix}_{\hat{\mathbf{x}}}^T \quad (A.3)
 \end{aligned}$$

and

$$\widetilde{M} = \partial \mathbf{h} / \partial \mathbf{v}|_{\hat{\mathbf{x}}} = \text{diag} \{[1, 1]\} \quad (\text{A.4})$$

, where $\partial i / \partial j$ denotes the derivative of i with respect to j , $i = p_{x,1}, p_{x,2}, p_{y,1}, p_{y,2}$ and $j = x_r, y_r, \varphi, x_1, y_1, x_2, y_2$. Then the derivative of $p_{x,1}$ in Eq. (4.13) with respect to x_r is derived as

$$\partial p_{x,1} / \partial x_r = p_{x,1,xr}^1 + p_{x,1,xr}^2 \quad (\text{A.5})$$

, where

$$p_{x,1,xr}^1 = - \frac{f_x \cos \varphi}{z_1' \cos \phi - b_y \sin \phi - x_1' \sin \phi \sin \varphi + y_1' \sin \phi \cos \varphi} \quad (\text{A.6})$$

and

$$p_{x,1,xr}^2 = - \frac{f_x \sin \phi \sin \varphi (x_1' \cos \varphi - b_x + y_1' \sin \varphi)}{(z_1' \cos \phi - b_y \sin \phi - x_1' \sin \phi \sin \varphi + y_1' \sin \phi \cos \varphi)^2} \quad (\text{A.7})$$

The derivative of $p_{x,2}$ in Eq. (4.14) with respect to x_r is

$$\partial p_{x,2} / \partial x_r = p_{x,2,xr}^1 + p_{x,2,xr}^2 \quad (\text{A.8})$$

, where

$$p_{x,2,xr}^1 = - \frac{f_x \cos \varphi}{z_2' \cos \phi - b_y \sin \phi - x_2' \sin \phi \sin \varphi + y_2' \sin \phi \cos \varphi} \quad (\text{A.9})$$

and

$$p_{x,2,xr}^2 = - \frac{f_x \sin \phi \sin \varphi (x_2' \cos \varphi - b_x + y_2' \sin \varphi)}{(z_2' \cos \phi - b_y \sin \phi - x_2' \sin \phi \sin \varphi + y_2' \sin \phi \cos \varphi)^2} \quad (\text{A.10})$$

The derivative of $p_{x,1}$ with respect to y_r is

$$\partial p_{x,1} / \partial y_r = p_{x,1,yr}^1 + p_{x,1,yr}^2 \quad (\text{A.11})$$

, where

$$p_{x,1,yr}^1 = -\frac{f_x \sin \phi}{z'_1 \cos \phi - b_y \sin \phi - x'_1 \sin \phi \sin \phi + y'_1 \sin \phi \cos \phi} \quad (\text{A.12})$$

and

$$p_{x,1,yr}^2 = \frac{f_x \sin \phi \cos \phi (x'_1 \cos \phi - b_x + y'_1 \sin \phi)}{(z'_1 \cos \phi - b_y \sin \phi - x'_1 \sin \phi \sin \phi + y'_1 \sin \phi \cos \phi)^2} \quad (\text{A.13})$$

The derivative of $p_{x,2}$ with respect to y_r is

$$\partial p_{x,2} / \partial y_r = p_{x,2,yr}^1 + p_{x,2,yr}^2 \quad (\text{A.14})$$

, where

$$p_{x,2,yr}^1 = -\frac{f_x \sin \phi}{z'_2 \cos \phi - b_y \sin \phi - x'_2 \sin \phi \sin \phi + y'_2 \sin \phi \cos \phi} \quad (\text{A.15})$$

and

$$p_{x,2,yr}^2 = \frac{f_x \sin \phi \cos \phi (x'_2 \cos \phi - b_x + y'_2 \sin \phi)}{(z'_2 \cos \phi - b_y \sin \phi - x'_2 \sin \phi \sin \phi + y'_2 \sin \phi \cos \phi)^2} \quad (\text{A.16})$$

The derivative of $p_{x,1}$ with respect to ϕ is

$$\partial p_{x,1} / \partial \phi = p_{x,1,\phi}^1 + p_{x,1,\phi}^2 \quad (\text{A.17})$$

, where

$$p_{x,1,\phi}^1 = -\frac{f_x (x'_1 \sin \phi - y'_1 \cos \phi)}{z'_1 \cos \phi - b_y \sin \phi - x'_1 \sin \phi \sin \phi + y'_1 \sin \phi \cos \phi} \quad (\text{A.18})$$

and

$$p_{x,1,\phi}^2 = \frac{f_x V_{x,\phi,1}}{(z'_1 \cos \phi - b_y \sin \phi - x'_1 \sin \phi \sin \phi + y'_1 \sin \phi \cos \phi)^2} \quad (\text{A.19})$$

, where

$$V_{x,\phi,1} = x'_1 \sin \phi \cos \phi + y'_1 \sin \phi \sin \phi (x'_1 \cos \phi - b_x + y'_1 \sin \phi) \quad (\text{A.20})$$

The derivative of $p_{x,2}$ with respect to φ is

$$\partial p_{x,2}/\partial \varphi = p_{x,2,\varphi}^1 + p_{x,2,\varphi}^2 \quad (\text{A.21})$$

, where

$$p_{x,2,\varphi}^1 = -\frac{f_x (x'_2 \sin \varphi - y'_2 \cos \varphi)}{z'_2 \cos \phi - b_y \sin \phi - x'_2 \sin \phi \sin \varphi + y'_2 \sin \phi \cos \varphi} \quad (\text{A.22})$$

and

$$p_{x,2,\varphi}^2 = \frac{f_x V_{x,\varphi,2}}{(z'_2 \cos \phi - b_y \sin \phi - x'_2 \sin \phi \sin \varphi + y'_2 \sin \phi \cos \varphi)^2} \quad (\text{A.23})$$

, where

$$V_{x,\varphi,2} = x'_2 \sin \phi \cos \varphi + y'_2 \sin \phi \sin \varphi (x'_2 \cos \varphi - b_x + y'_2 \sin \varphi) \quad (\text{A.24})$$

The derivative of $p_{x,1}$ with respect to x_1 is derived as

$$\partial p_{x,1}/\partial x_1 = p_{x,1,x_1}^1 + p_{x,1,x_1}^2 \quad (\text{A.25})$$

, where

$$p_{x,1,x_1}^1 = \frac{f_x \cos \varphi}{z'_1 \cos \phi - b_y \sin \phi - x'_1 \sin \phi \sin \varphi + y'_1 \sin \phi \cos \varphi} \quad (\text{A.26})$$

and

$$p_{x,1,x_1}^2 = \frac{f_x \sin \phi \sin \varphi (x'_1 \cos \varphi - b_x + y'_1 \sin \varphi)}{(z'_1 \cos \phi - b_y \sin \phi - x'_1 \sin \phi \sin \varphi + y'_1 \sin \phi \cos \varphi)^2} \quad (\text{A.27})$$

The derivative of $p_{x,2}$ with respect to x_1 is derived as

$$\partial p_{x,2}/\partial x_1 = 0 \quad (\text{A.28})$$

The derivative of $p_{x,1}$ with respect to y_1 is derived as

$$\partial p_{x,1}/\partial y_1 = p_{x,1,y_1}^1 + p_{x,1,y_1}^2 \quad (\text{A.29})$$

, where

$$p_{x,1,y_1}^1 = \frac{f_x \sin \varphi}{z_1' \cos \phi - b_y \sin \phi - x_1' \sin \phi \sin \varphi + y_1' \sin \phi \cos \varphi} \quad (\text{A.30})$$

and

$$p_{x,1,y_1}^2 = -\frac{f_x \sin \phi \cos \varphi (x_1' \cos \varphi - b_x + y_1' \sin \varphi)}{(z_1' \cos \phi - b_y \sin \phi - x_1' \sin \phi \sin \varphi + y_1' \sin \phi \cos \varphi)^2} \quad (\text{A.31})$$

The derivative of $p_{x,2}$ with respect to y_1 is derived as

$$\partial p_{x,2}/\partial y_1 = 0 \quad (\text{A.32})$$

The derivative of $p_{x,1}$ with respect to x_2 is derived as

$$\partial p_{x,1}/\partial x_2 = 0 \quad (\text{A.33})$$

The derivative of $p_{x,2}$ with respect to x_2 is derived as

$$\partial p_{x,2}/\partial x_2 = p_{x,2,x_2}^1 + p_{x,2,x_2}^2 \quad (\text{A.34})$$

, where

$$p_{x,2,x_2}^1 = \frac{f_x \cos \varphi}{z_2' \cos \phi - b_y \sin \phi - x_2' \sin \phi \sin \varphi + y_2' \sin \phi \cos \varphi} \quad (\text{A.35})$$

and

$$p_{x,2,x_2}^2 = \frac{f_x \sin \varphi \sin \phi (x_2' \cos \varphi - b_x + y_2' \sin \varphi)}{(z_2' \cos \phi - b_y \sin \phi - x_2' \sin \phi \sin \varphi + y_2' \sin \phi \cos \varphi)^2} \quad (\text{A.36})$$

The derivative of $p_{x,1}$ with respect to y_2 is derived as

$$\partial p_{x,1}/\partial y_2 = 0 \quad (\text{A.37})$$

The derivative of $p_{x,2}$ with respect to y_2 is derived as

$$\partial p_{x,2}/\partial y_2 = p_{x,2,y_2}^1 + p_{x,2,y_2}^2 \quad (\text{A.38})$$

, where

$$p_{x,2,y_2}^1 = \frac{f_x \sin \varphi}{z_2' \cos \phi - b_y \sin \phi - x_2' \sin \phi \sin \varphi + y_2' \sin \phi \cos \varphi} \quad (\text{A.39})$$

and

$$p_{x,2,y_2}^2 = -\frac{f_x \sin \phi \cos \varphi (x_2' \cos \varphi - b_x + y_2' \sin \varphi)}{(z_2' \cos \phi - b_y \sin \phi - x_2' \sin \phi \sin \varphi + y_2' \sin \phi \cos \varphi)^2} \quad (\text{A.40})$$

The derivative of $p_{y,2}$ in Eq. (4.16) with respect to x_r is

$$\partial p_{y,2}/\partial x_r = p_{y,2,xr}^1 + p_{y,2,xr}^2 \quad (\text{A.41})$$

, where

$$p_{y,2,xr}^1 = -\frac{f_y \cos \phi \sin \varphi}{z_2' \cos \phi - b_y \sin \phi - x_2' \sin \phi \sin \varphi + y_2' \sin \phi \cos \varphi} \quad (\text{A.42})$$

and

$$p_{y,2,xr}^2 = -\frac{f_y V_{y,\varphi,2} \sin \phi \sin \varphi}{(z_2' \cos \phi - b_y \sin \phi - x_2' \sin \phi \sin \varphi + y_2' \sin \phi \cos \varphi)^2} \quad (\text{A.43})$$

, where

$$V_{y,\varphi,2} = z_2' \sin \phi - b_y \cos \phi + x_2' \cos \phi \sin \varphi - y_2' \cos \phi \cos \varphi \quad (\text{A.44})$$

The derivative of $p_{y,1}$ in Eq. (4.15) with respect to x_r is

$$\partial p_{y,1}/\partial x_r = p_{y,1,xr}^1 + p_{y,1,xr}^2 \quad (\text{A.45})$$

, where

$$p_{y,1,xr}^1 = -\frac{f_y \cos \phi \sin \varphi}{z'_1 \cos \phi - b_y \sin \phi - x'_1 \sin \phi \sin \varphi + y'_1 \sin \phi \cos \varphi} \quad (\text{A.46})$$

and

$$p_{y,1,xr}^2 = -\frac{f_y V_{y,\varphi,1} \sin \phi \sin \varphi}{(z'_1 \cos \phi - b_y \sin \phi - x'_1 \sin \phi \sin \varphi + y'_1 \sin \phi \cos \varphi)^2} \quad (\text{A.47})$$

, where

$$V_{y,\varphi,1} = z'_1 \sin \phi - b_y \cos \phi + x'_1 \cos \phi \sin \varphi - y'_1 \cos \phi \cos \varphi \quad (\text{A.48})$$

The derivative of $p_{y,2}$ with respect to y_r is

$$\partial p_{y,2}/\partial y_r = p_{y,2,yr}^1 + p_{y,2,yr}^2 \quad (\text{A.49})$$

, where

$$p_{y,2,yr}^1 = \frac{f_y \cos \phi \cos \varphi}{z'_2 \cos \phi - b_y \sin \phi - x'_2 \sin \phi \sin \varphi + y'_2 \sin \phi \cos \varphi} \quad (\text{A.50})$$

and

$$p_{y,2,yr}^2 = \frac{f_y V_{y,\varphi,2} \sin \phi \cos \varphi}{(z'_2 \cos \phi - b_y \sin \phi - x'_2 \sin \phi \sin \varphi + y'_2 \sin \phi \cos \varphi)^2} \quad (\text{A.51})$$

The derivative of $p_{y,1}$ with respect to y_r is

$$\partial p_{y,1}/\partial y_r = p_{y,1,yr}^1 + p_{y,1,yr}^2 \quad (\text{A.52})$$

, where

$$p_{y,1,yr}^1 = \frac{f_y \cos \phi \cos \varphi}{z'_1 \cos \phi - b_y \sin \phi - x'_1 \sin \phi \sin \varphi + y'_1 \sin \phi \cos \varphi} \quad (\text{A.53})$$

and

$$p_{y,1,yr}^2 = \frac{f_y V_{y,\varphi,1} \sin \phi \cos \varphi}{(z'_1 \cos \phi - b_y \sin \phi - x'_1 \sin \phi \sin \varphi + y'_1 \sin \phi \cos \varphi)^2} \quad (\text{A.54})$$

The derivative of $p_{y,2}$ with respect to φ is

$$\partial p_{y,2} / \partial \varphi = p_{y,2,\varphi}^1 + p_{y,2,\varphi}^2 \quad (\text{A.55})$$

, where

$$p_{y,2,\varphi}^1 = \frac{f_y (x'_2 \cos \phi \cos \varphi + y'_2 \cos \phi \sin \varphi)}{z'_2 \cos \phi - b_y \sin \phi - x'_2 \sin \phi \sin \varphi + y'_2 \sin \phi \cos \varphi} \quad (\text{A.56})$$

and

$$p_{y,2,\varphi}^2 = \frac{f_y V_{y,\varphi,2} (x'_2 \sin \phi \cos \varphi + y'_2 \sin \phi \sin \varphi)}{(z'_2 \cos \phi - b_y \sin \phi - x'_2 \sin \phi \sin \varphi + y'_2 \sin \phi \cos \varphi)^2} \quad (\text{A.57})$$

The derivative of $p_{y,1}$ with respect to φ is

$$\partial p_{y,1} / \partial \varphi = p_{y,1,\varphi}^1 + p_{y,1,\varphi}^2 \quad (\text{A.58})$$

, where

$$p_{y,1,\varphi}^1 = \frac{f_y (x'_1 \cos \phi \cos \varphi + y'_1 \cos \phi \sin \varphi)}{z'_1 \cos \phi - b_y \sin \phi - x'_1 \sin \phi \sin \varphi + y'_1 \sin \phi \cos \varphi} \quad (\text{A.59})$$

and

$$p_{y,1,\varphi}^2 = \frac{f_y V_{y,\varphi,1} (x'_1 \sin \phi \cos \varphi + y'_1 \sin \phi \sin \varphi)}{(z'_1 \cos \phi - b_y \sin \phi - x'_1 \sin \phi \sin \varphi + y'_1 \sin \phi \cos \varphi)^2} \quad (\text{A.60})$$

The derivative of $p_{y,2}$ with respect to x_1 is

$$\partial p_{y,2}/\partial x_1 = 0 \quad (\text{A.61})$$

The derivative of $p_{y,1}$ with respect to x_1 is

$$\partial p_{y,1}/\partial x_1 = p_{y,1,x1}^1 + p_{y,1,x1}^2 \quad (\text{A.62})$$

, where

$$p_{y,1,x1}^1 = \frac{f_y \cos \phi \sin \varphi}{z_1' \cos \phi - b_y \sin \phi - x_1' \sin \phi \sin \varphi + y_1' \sin \phi \cos \varphi} \quad (\text{A.63})$$

and

$$p_{y,1,x1}^2 = \frac{f_y V_{y,\varphi,1} \sin \phi \sin \varphi}{(z_1' \cos \phi - b_y \sin \phi - x_1' \sin \phi \sin \varphi + y_1' \sin \phi \cos \varphi)^2} \quad (\text{A.64})$$

The derivative of $p_{y,2}$ with respect to y_1 is

$$\partial p_{y,2}/\partial y_1 = 0 \quad (\text{A.65})$$

The derivative of $p_{y,1}$ with respect to y_1 is

$$\partial p_{y,1}/\partial y_1 = p_{y,1,y1}^1 + p_{y,1,y1}^2 \quad (\text{A.66})$$

, where

$$p_{y,1,y1}^1 = \frac{f_y \cos \phi \cos \varphi}{z_1' \cos \phi - b_y \sin \phi - x_1' \sin \phi \sin \varphi + y_1' \sin \phi \cos \varphi} \quad (\text{A.67})$$

and

$$p_{y,1,y1}^2 = \frac{f_y V_{y,\varphi,1} \sin \phi \cos \varphi}{(z_1' \cos \phi - b_y \sin \phi - x_1' \sin \phi \sin \varphi + y_1' \sin \phi \cos \varphi)^2} \quad (\text{A.68})$$

The derivative of $p_{y,2}$ with respect to x_2 is

$$\partial p_{y,2}/\partial x_2 = p_{y,2,x_2}^1 + p_{y,2,x_2}^2 \quad (\text{A.69})$$

, where

$$p_{y,2,x_2}^1 = \frac{f_y \cos \phi \sin \varphi}{z'_2 \cos \phi - b_y \sin \phi - x'_2 \sin \phi \sin \varphi + y'_2 \sin \phi \cos \varphi} \quad (\text{A.70})$$

and

$$p_{y,2,x_2}^2 = \frac{f_y V_{y,\varphi,2} \sin \phi \sin \varphi}{(z'_2 \cos \phi - b_y \sin \phi - x'_2 \sin \phi \sin \varphi + y'_2 \sin \phi \cos \varphi)^2} \quad (\text{A.71})$$

The derivative of $p_{y,1}$ with respect to x_2 is

$$\partial p_{y,1}/\partial x_2 = 0 \quad (\text{A.72})$$

The derivative of $p_{y,2}$ with respect to y_2 is

$$\partial p_{y,2}/\partial y_2 = p_{y,2,y_2}^1 + p_{y,2,y_2}^2 \quad (\text{A.73})$$

, where

$$p_{y,2,y_2}^1 = \frac{f_y \cos \phi \cos \varphi}{z'_2 \cos \phi - b_y \sin \phi - x'_2 \sin \phi \sin \varphi + y'_2 \sin \phi \cos \varphi} \quad (\text{A.74})$$

and

$$p_{y,2,y_2}^2 = \frac{f_y V_{y,\varphi,2} \sin \phi \cos \varphi}{(z'_2 \cos \phi - b_y \sin \phi - x'_2 \sin \phi \sin \varphi + y'_2 \sin \phi \cos \varphi)^2} \quad (\text{A.75})$$

The derivative of $p_{y,1}$ with respect to y_2 is

$$\partial p_{y,1}/\partial y_2 = 0 \quad (\text{A.76})$$

LIST OF REFERENCES

- [1] Grand View Research, 2017, “Precision Agriculture Market Analysis by Component (Hardware, Software & Services), by Technology Variable Rate Technology, Remote Sensing, Guidance Systems, by Application, by Region, and Segment Forecasts, 2014-2025,” Jan., Report No. 4717549.
- [2] Rouphael, Y., Spchal, L., Panzarov, K., Casa, R., and Colla, G., 2018, “High-Throughput Plant Phenotyping for Developing Novel Biostimulants: From Lab to Field or From Field to Lab?,” *Front. Plant. Sci.*, **9**, Article 1197.
- [3] Borenstein, J., Everett, H. R., Feng, L., and Wehe, D., 1997, “Mobile Robot Positioning: Sensors and Techniques,” *J. Intell. Robot Syst.*, **14**(4), pp. 231-249.
- [4] Herrero-Pérez, D., Martinez-Barberá, H., LeBlanc, K., and Saffiotti, A., 2010, “Fuzzy Uncertainty Modeling for Grid Based Localization of Mobile Robots,” *Int. J. Approx. Reason.*, **51**(8), pp. 912-932.
- [5] Joerger, M., and Pervan, B., 2009, “Measurement-level Integration of Carrier-phase GPS and Laser-Scanner for Outdoor Ground Vehicle Navigation,” *ASME J. Dyn. Sys., Meas., Control*, **131**(2), pp. 021004.
- [6] Ryu, J., and Gerdes, J. C., 2004, “Integrating Inertial Sensors With Global Positioning System (GPS) for Vehicle Dynamics Control,” *ASME J. Dyn. Sys., Meas., Control*, **126**(2), pp. 243-254.
- [7] Dawkins, J. J., 2017, “Relative Position Estimation Using Monocular Camera and Ultra-Wide Band Ranging,” *ASME 2017 Dynamic Systems and Control Conference*, Tysons, Virginia, Oct. 11-13.

- [8] Sun, H., Slaughter, D. C., Ruiz, M. P., Gliever, C., Upadhyaya, S. K., and Smith, R. F., 2010, "RTK GPS Mapping of Transplanted Row Crops," *Comput. Electron. Agr.*, **71**(1), pp. 32-37.
- [9] Garrido, M., Perez-Ruiz, M., Valero, C., Gliever, C. J., Hanson, B. D., and Slaughter, D. C., 2014, "Active Optical Sensors for Tree Stem Detection and Classification in Nurseries," *Sensors*, **14**(6), pp. 10783-10803.
- [10] Kim, J. S., Kim, A. H., Oh, H. B., Goh, B. J., Lee, E. S., Kim, J. S., Jung, G. I., Baek, J. Y., and Jun, J. H., 2015, "Simple LED Spectrophotometer for Analysis of Color Information," *Biomed. Mater. Eng.*, **26**(s1), pp. 1773-1780.
- [11] Gonzalez, R. C., and Woods, R. E., 2008, *Digital Image Processing*, Pearson Education Inc., Upper Saddle River, New Jersey.
- [12] Li, X., Lee, W. S., Li, M., Ehsani, R., Mishra, A. R., Yang, C., and Mangan, R. L., 2012, "Spectral Difference Analysis and Airborne Imaging Classification for Citrus Greening Infected Trees," *Comput. Electron. Agr.*, **83**, pp. 32-46.
- [13] Garcia-Ruiz, F., Sankaran, S., Maja, J. M., Lee, W. S., Rasmussen, J., and Ehsani, R., 2013, "Comparison of Two Aerial Imaging Platforms for Identification of Huanglongbing-Infected Citrus Trees," *Comput. Electron. Agr.*, **91**, pp. 106-115.
- [14] Patil, J. K., and Kumar, R., 2011, "Advances in Image Processing for Detection of Plant Diseases," *J. Adv. Bioinformatics Appl. Res.*, **2**(2), pp. 135-141.
- [15] Du, C. J., and Sun, D. W., 2004, "Recent Developments in the Applications of Image Processing Techniques for Food Quality Evaluation," *Trends Food Sci. Technol.*, **15**(5), pp. 230-249.
- [16] Abbott, J. A., 1999, "Quality Measurement of Fruits and Vegetables," *Postharvest Biol. Technol.*, **15**(3), pp. 207-225.

- [17] Kulkarni, N., 2012, "Color Thresholding Method for Image Segmentation of Natural Images," *Int. J. Image, Graphics, Signal Process.*, **1**, pp. 28-34.
- [18] Yang, W., Wang, S., Zhao, X., Zhang, J., and Feng, J., 2015, "Greenness Identification Based on HSV Decision Tree," *Inf. Process. Agr.*, **2**(3-4), pp. 149-160.
- [19] Sammouda, R., Adgaba, N., Touir, A., and Al-Ghamdi, A., 2014, "Agriculture Satellite Image Segmentation Using a Modified Artificial Hopfield Neural Network," *Comput. Human Behav.*, **30**, pp. 436-441.
- [20] Jhuria, M., Kumar, A., and Borse, R., 2013, "Image Processing for Smart Farming: Detection of Disease and Fruit Grading," 2013 IEEE Second International Conference on Image Information Processing, Shimla, India, Dec. 9-11.
- [21] Meyer, G. E., Neto, J. C., Jones, D. D., and Hindman, T. W., 2004, "Intensified Fuzzy Clusters for Classifying Plant, Soil, and Residue Regions of Interest from Color Images," *Comput. Electron. Agr.*, **42**(3), pp. 161-180.
- [22] Agro Services International, Inc. "Balanced Nutrition" Available at: <https://www.agroservicesinternational.com/Balanced/What%20is%20balanced.html>
- [23] PennState Extension, 2018, "Scouting for Nutrition Deficiencies" Available at: <https://extension.psu.edu/scouting-for-nutrient-deficiencies>
- [24] Uchida, R., 2000, "Essential Nutrients for Plant Growth: Nutrient Functions and Deficiency Symptoms," *Plant nutrient management in Hawaii soils*, pp. 31–55.
- [25] Tyner, E. H., and Webb, J. R., 1946, "Relation of Corn Yields to Nutrient Balance as Revealed by Leaf Analysis," *Journal of the American Society of Agronomy*.
- [26] Besford, R. T., 1980, "A Rapid Tissue Test for Diagnosing Phosphorus Deficiency in the Tomato Plant," *Annals of Botany*, **45**(2), pp. 225–227.

- [27] Cress, W. A., Throneberry, G. O., and Lindsey, D. L., 1979, “Kinetics of Phosphorus Absorption by Mycorrhizal and Nonmycorrhizal Tomato Roots,” *Plant Physiology*, **64**(3), pp. 484–487.
- [28] Lineberry, R. A., and Burkhart, L., 1943, “Nutrient Deficiencies in the Strawberry Leaf and Fruit,” *Plant Physiology*, **18**(3), pp. 324.
- [29] Yara UK Limited, “Nutrition Deficiencies-Strawberry” Available at: <https://www.yara.co.uk/crop-nutrition/strawberries/nutrient-deficiencies-strawberry/>
- [30] KeyPlex, “Determining N, P, K Deficiencies in Strawberries through Visual ObservationsNutrition Deficiencies-Strawberry” Available at: <https://www.keyplex.com/knowledge-base/strawberry-research/how-to-recognize-nitrogen-phosphorous-and-potassium-deficiencies-in-strawberries/>
- [31] Sun, Y., Zhu, S., Yang, X., Weston, M. V., Wang, K., Shen, Z., Xu, H., and Chen, L., 2018, “Nitrogen Diagnosis Based on Dynamic Characteristics of Rice Leaf Image,” *PloS one*, **13**(4), pp. e0196298.
- [32] Yu, K., Zhao, Y., Li, X., Shao, Y., Liu, F., and He, Y., 2014, “Hyperspectral Imaging for Mapping of Total Nitrogen Spatial Distribution in Pepper Plant,” , **9**(12), pp. e116205.
- [33] Vigneau, N., Ecartot, M., Rabatel, G., and Roumet, P., 2011, “Potential of Field Hyperspectral Imaging as a Non Destructive Method to Assess Leaf Nitrogen Content in Wheat,” *Field Crops Research*, **122**(1), pp. 25–31.
- [34] Ulrich, A., Mostafa, M., and Allen, W. W. C., 1992, *Strawberry Deficiency Symptoms: A Visual and Plant Analysis Guide to Fertilization*, University of California.

- [35] Kong, X., and Xu, Y., 2019, "Strawberry Plant Alive Status Detection and Relative Pixel Based Plant Localization," submitted to the ASME Journal of Dynamic System, Measurement, and Control in Jan, 2019
- [36] Smith, A. R., 1978, "Color Gamut Transform Pairs," ACM Siggraph Computer Graphics, **12**(3), pp. 12-19.
- [37] Hitam, M. S., Awalludin, E. A., Jawahir Hj Wan Yussof, W. N., and Bachok, Z., 2013, "Mixture Contrast Limited Adaptive Histogram Equalization for Underwater Image Enhancement," 2013 International Conference on Computer Applications Technology, Sousse, Tunisia, Jan. 20-22.
- [38] Martian Color Wheel, 2014, "Martian 24 Hue Color Wheel," Available at: warrenmars.com/visual_art/theory/colour_wheel/colour_wheel.htm
- [39] Kaur, S., and Banga, D. V. K., 2013, "Content Based Image Retrieval: Survey and Comparison between RGB and HSV Model," Int. J. Eng. Trends Technol., **4**(4), pp. 575-579.
- [40] Glas, A. S., Lijmer, J. G., Prins, M. H., Bonsel, G. J., and Bossuyt, P. M., 2003, "The Diagnostic Odds Ratio: A Single Indicator of Test Performance," J. Clin. Epidemiol., **56**(11), pp. 1129-1135.
- [41] Pearce, J., and Ferrier, S., 2000, "Evaluating the Predictive Performance of Habitat Models Developed Using Logistic Regression," Ecol. Modell., **133**(3), pp. 225-245.
- [42] Louhaichi, M., Borman, M. M., and Johnson, D. E., 2000, "Spatially Located Platform and Aerial Photography for Documentation of Grazing Impacts on Wheat," Geocarto. Int., **16**(1), pp. 65-70.

- [43] Miyanawala, T. P., and Jaiman, R. K., 2018, "A Novel Deep Learning Method for the Predictions of Current Forces on Bluff Bodies," ASME 2018 37th International Conference on Ocean, Offshore and Arctic Engineering, Madrid, Spain, June 17-22.
- [44] Kong, X., and Xu, Y., 2018, "Strawberry Plant Localization via Relative Pixels in Sequential Images," ASME 2018 Dynamic Systems and Control Conference, Atlanta, Georgia, Sep. 30 - Oct. 3.
- [45] Freese, D., and Xu, Y., 2017, "Nonlinear Robust Path Control for a Field Robot Scouting in Strawberry Orchards," ASME 2017 Dynamic Systems and Control Conference, Tysons, Virginia, Oct. 11-13.
- [46] Simon, D., 2006, *Optimal State Estimation: Kalman, H Infinity, and Nonlinear Approaches*, John Wiley & Sons, Inc., Hoboken, New Jersey.
- [47] Wong, X. I., and Majji, M., 2018, "Extended Kalman Filter for Stereo Vision-Based Localization and Mapping Applications," ASME J. Dyn. Sys., Meas., Control, **140**(3), pp. 030908.
- [48] Gudmundsson, V., Kristinsson, H., Petersen, S., and Hasan, A., 2018, "Robust UAV Attitude Estimation Using a Cascade of Nonlinear Observer and Linearized Kalman Filter," ASME 2018 Dynamic Systems and Control Conference, Atlanta, Georgia, Sep. 30 - Oct. 3.
- [49] Menendez-Aponte, P., Garcia, C., Freese, D., Defterli, S., and Xu, Y., 2016, "Software and Hardware Architectures in Cooperative Aerial and Ground Robots for Agricultural Disease Detection," International Conference on Collaboration Technologies and Systems, Orlando, Florida, Oct. 31 - Nov. 4.
- [50] Zhang, J., and Chen, Y., and Huang, X., 2009, "Edge Detection of Images Based on Improved Sobel Operator and Genetic Algorithms," 2009 International Conference on Image Analysis and Signal Processing, pp. 31–35.

- [51] Tomasi, C., and Manduchi, R., 1998, “Bilateral filtering for gray and color images,” *Iccc*, **98**(1), pp. 2.
- [52] Deng, G., and Cahill, L. W., 1993, “An Adaptive Gaussian Filter for Noise Reduction and Edge Detection,” 1993 IEEE Conference Record Nuclear Science Symposium and Medical Imaging Conference, pp. 1615–1619.
- [53] Kanopoulos, N., Vasanthavada, N., and Baker, R. L., 1988, “Design of An Image Edge Detection Filter using the Sobel Operator,” *IEEE J. Solid-State Circuits*, **23**(2), pp. 358–367.
- [54] Reuter, M., Biasotti, S., Giorgi, D., Patanè, G., and Spagnuolo, M., 2009, “Discrete Laplace–Beltrami Operators for Shape Analysis and Segmentation,” *Computers & Graphics*, **33**(3), pp. 381–390.
- [55] Chaple, G. N., Daruwala, R. D. and Gofane, M. S., 2015, “Comparisions of Robert, Prewitt, Sobel Operator based Edge Detection Methods for Real Time Uses on FPGA,” 2015 International Conference on Technologies for Sustainable Development (ICTSD), pp. 1–4.
- [56] Qu, Y., Cui, C., and Chen, S., and Li, J., 2005, “A Fast Subpixel Edge Detection Method using Sobel–Zernike Moments Operator,” *Image Vis Comput.* , **23**(1), pp. 11–17.
- [57] Goutte, C., and Gaussier, E., 2005, “A Probabilistic Interpretation of Precision, Recall and F-score, with Implication for Evaluation,” *European Conference on Information Retrieval.*, pp. 345–359.
- [58] Menendez-Aponte, P., Kong, X., and Xu, Y., 2019, “An Approximated, Control Affine Model for a Strawberry Field Scouting Robot Considering Wheel-Terrain Interaction,” *Robotica.* , pp. 1–17.

- [59] Menendez-Aponte, P., 2016, “Approximated Control Affine Dynamics Model for an Agricultural Field Robot Considering Wheel Terrain Interaction,” Master Thesis, University of Central Florida, Orlando, FL.
- [60] Tran, T. H., Kwok, N. M., Scheduling, S., and Ha, Q. P., 2007, “Dynamic Modeling of Wheel-Terrain Interaction of a UGV,” The 3rd IEEE International Conference on Automation Science and Engineering, pp. 369–374.
- [61] Jia, Z., Smith, W., and Peng, H., 2011, “Terramechanics-based Wheelterrain Interaction Model and Its Applications to Off-road Wheeled Mobile Robots,” *Robotica*, **30**(3), pp. 491–503.
- [62] Wong, J. Y., 2001, *Theory of Ground Vehicles*, John Wiley & Sons.
- [63] Ward, C. C., and Iagnemma, K., 2008, “A Dynamic-Model-Based Wheel Slip Detector for Mobile Robots on Outdoor Terrain,” *IEEE Trans. Robot.*, **24**(4), pp. 821–831.
- [64] Yi, J., Wang, H., Zhang, J., Song, D., Jayasuriya, S., and Liu, J., 2009, “Kinematic Modeling and Analysis of Skid-Steered Mobile Robots with Applications to Low-Cost Inertial-Measurement-Unit-Based Motion Estimation,” *IEEE Trans. Robot.*, **25**(5), pp. 1087–1097.
- [65] Ishigami, G., Miwa, A., Nagatani, K., and Yoshida, K., 2007, “Terramechanics-based Model for Steering Maneuver of Planetary Exploration Rovers on Loose Soil,” *J FIELD ROBOT.*, **24**(3), pp. 233–250.
- [66] Wong, J., and Reece, A. R., 1967, “Prediction of Rigid Wheel Performance Based on the Analysis of Soil-Wheel Stresses: Part II. Performance of Towed Rigid Wheels,” *Journal of Terramechanics*, **4**(2), pp. 7–25.

- [67] Yi, J., Song, D., Zhang, J., and Goodwin, Z., 2007, “Adaptive Trajectory Tracking Control of Skid-Steered Mobile Robots,” 2007 IEEE International Conference on Robotics and Automation, pp. 2605–2610.
- [68] Onafeko, O., and Reece, A. R., 1967, “Soil Stresses and Deformations Beneath Rigid Wheels,” *Journal of Terramechanics*, **4**(1), pp. 59–80.
- [69] Caracciolo, L., De Luca, A., and Iannitti, S., 1999, “Trajectory Tracking Control of a Four-Wheel Differentially Driven Mobile Robot,” *IEEE International Conference on Robotics and Automation*, **4**, pp. 2632–2638.